

Bayesian fitting of Taurus brown dwarf spectral energy distributions

N.J. Mayne^{*}, Tim J. Harries, John Rowe and David M. Acreman

School of Physics, University of Exeter, Stocker Road, Exeter, EX4 4QL.

Accepted ?. Received ?; in original form ?

ABSTRACT

We present derived stellar and disc parameters for a sample of Taurus brown dwarfs both with and without evidence of an associated disc. These parameters have been derived using an online fitting tool (<http://bd-server.astro.ex.ac.uk/>), which includes a statistically robust derivation of uncertainties, an indication of parameter degeneracies, and a complete treatment of the input photometric and spectroscopic observations.

The observations of the Taurus members with indications of disc presence have been fitted using a grid of theoretical models including detailed treatments of physical processes accepted for higher mass stars, such as dust sublimation, and a simple treatment of the accretion flux. This grid of models has been designed to test the validity of the adopted physical mechanisms, but we have also constructed models using parameterisation, for example semi-empirical dust sublimation radii, for users solely interested in parameter derivation and the quality of the fit.

The parameters derived for the naked and disc brown dwarf systems are largely consistent with literature observations. However, our inner disc edge locations are consistently closer to the star than previous results and we also derive elevated accretion rates over non-SED based accretion rate derivations. For inner edge locations we attribute these differences to the detailed modelling we have performed of the disc structure, particularly at the crucial inner edge where departures in geometry from the often adopted vertical wall due to dust sublimation (and therefore accretion flux) can compensate for temperature (and therefore distance) changes to the inner edge of the dust disc. In the case of the elevated derived accretion rates, in some cases, this may be caused by the intrinsic stellar luminosities of the targets exceeding that predicted by the isochrones we have adopted.

Key words: stars:evolution – stars:formation – stars: pre-main-sequence – techniques: photometric – catalogues – (stars) Hertzsprung-Russell H-R diagram

1 INTRODUCTION

In studies of star formation and evolution spectral energy distribution (SED) fitting is often used to derive parameters for stars and their circumstellar discs. Fitting tools, such as Robitaille et al. (2006), and the increasing availability of observational data have led to a rapid increase in the number of studies using SED fitting. As observations of fainter lower-mass stars (LMS) and brown dwarfs (BDs) have become feasible (see for example Jayawardhana et al. 2003; Luhman et al. 2005, 2008; Guieu et al. 2007; Monin et al. 2010; Olofsson et al. 2010) such SED fitting techniques have

been extended into the lower mass regime. These studies have generally been limited to small numbers of members of the Taurus star forming region (SFR) due to its proximity.

For higher mass stars extensive studies have been performed using detailed treatments of the important physical processes, for example radiative transfer, dust sublimation and vertical hydrostatic equilibrium (see for example Tannirkulam et al. 2008; Walker et al. 2004). Such models are computationally expensive and as such are usually used to model individual systems. The online fitting tool of Robitaille et al. (2006) has allowed much greater access to such models via pre-computed ‘grids’ of radiative transfer simulations covering a selected parameter space, for example a range of masses and ages. However, the young-stellar objects

* E-mail: nathan@astro.ex.ac.uk (NJM)

(YSOs) modelled by Robitaille et al. (2006) do not extend into the BD mass regime.

In the low mass regime, studies of populations of objects are generally performed using parameterisations of physical mechanisms rendering the problem computationally tractable. χ^2 fitting is used to derive parameters from a grid of model SEDs computed over ranges of parameters selected by the user (e.g. Bouy et al. 2008; Monin et al. 2010; Olofsson et al. 2010). For example, the inner boundary of the associated dust disc can be placed at a range of positions, the resulting SEDs derived, and the best fitting model selected, leading to an estimate of the inner edge radius. However, it is known that the flux from the inner edge is a complicated function of its geometry, composition and temperature, all of which can change as a function of the stellar properties (see discussion in Mayne & Harries 2010). A clear correlation between the observed inner edge location and the dust sublimation radius has been found for higher mass stars (Monnier & Millan-Gabet 2002). Our approach in this work is to constrain our modelling of BD and disc (BDD, hereafter) systems by adopting the physical mechanisms that have proved successful on their higher mass counterparts such as Classical T Tauri stars and Herbig Ae stars: (i) we constrain our disc structures so that they are in vertical hydrostatic equilibrium. (ii) The inner edge of the gas disc is truncated at the co-rotation radius (as such it is a function of stellar mass and rotational period, Camenzind 1990; Koenigl 1991; Muzerolle et al. 2003; Mohanty & Shu 2008). (iii) The location of the dust disc inner radius is defined dust sublimation (Tannirkulam et al. 2008). (iv) The photosphere luminosity is enhanced by accretion luminosity from material impacting on the BD surface (Bouvier et al. 1995; Herbst et al. 2007). Note that although we are apparently increasing the physical complexity of the model, we are in fact reducing the number of free parameters. As a consequence of this adequate fits to the SEDs act to corroborate the physical assumptions that underly our models, whilst inadequate fits lead us to question them. In contrast allowing (for example) the the disc structure to vary arbitrarily will necessarily result in an improved spectral fit, but perhaps at the cost of physical insight. Applying such models to the studies of populations then requires sufficient computing resource, or an available repository of pre-computed models.

Comparison of data and models is further complicated by temporal variability. Simulations of the dynamics of circumstellar discs have suggested that several mechanisms can lead to structural variations over a range of timescales, some as short as a few days (Min et al. 2009; Acreman et al. 2010). Combined with variations in emissions from the stellar photosphere from processes such as accretion (Bouvier et al. 1995; Herbst et al. 2007), this leads to significant variations in the observable properties. However, non-contemporaneous photometric data sets are often combined and fitted to derived SEDs, without consideration of such temporal variability. Additionally, previous studies have found that the optical photometry of BDs and LMS, which is vital for constraining the stellar parameters, are poorly represented by simulated stellar atmospheres. Furthermore, as the slope of the SED across the optical regime is much steeper than for higher mass systems, these measurements dominate the χ^2 value for a given fit and so are often

omitted from the fit (see for example Guieu et al. 2007). Discrepancies in the optical photometry, however, are often the result of converting magnitudes to a standard photometric system (to match the models), or indeed converting magnitudes to monochromatic fluxes, using simple transformations or calibrations. Such transformations are usually only accurate for main-sequence (MS) stars, and their use will introduce additional uncertainty in the observed BD fluxes.

We have used the TORUS radiative transfer code to simulate a large number of BDD systems covering a range of input parameters and adopting mechanisms accepted for higher mass systems. These simulations include a representation of dust sublimation, vertical hydrostatic equilibrium, accretion flux and radiative transfer. These models have been incorporated into an online fitting tool freely accessible to the community at <http://bd-server.astro.ex.ac.uk/>. This fitting tool includes an accurate treatment of the observational photometry so that it can be compared consistently with the simulated observations. As a proof of concept, and to aid development of this tool, we have fitted a sample of Taurus BD and BDD observations collected from the literature, the results of which we present in this paper. We have explored differences in our derived parameters from those in the literature and discuss some specific examples.

This paper is structured as follows. Section 2 introduces the adopted data-set for the sample of Taurus BDs and BDDs. The detail of the transformations and generation of uncertainties (the latter to be applied to the model during fitting) are mentioned in this section and explained in full in Appendix A. The models used, including the physics represented, are detailed in Section 3 alongside the fitting statistics and fitting process. Details of the calibration of the models and simulated observables are explained in full in Appendix B where the online interface and tools are also described. The results of the fitting are presented in Section 4 where we also discuss individual objects and comparison with other works. Finally we conclude in Section 6.

2 THE DATA

We have selected and fitted a sample of LMS and BDs from Taurus presented in Guieu et al. (2007). Guieu et al. (2007) present photometry for these objects and split them into those stars with infrared excesses (and by inference discs) and those without. For the purpose of this study we have used the same division. We have also performed a literature search for photometry and derived parameters of these objects. This has allowed us to develop an understanding of how to model the uncertainties of our models during fitting and to explore temporal variations in the observations.

Table 1 shows the short name used in this work and the 2MASS identification (from which the coordinates are easily found) to facilitate cross matching. Table 2 shows the adopted photometry for each of our target objects and their sources.

Table 2 also lists our estimates of the uncertainties for each observation. The uncertainties are not simply the values presented alongside the observations but also include components which attempt to account for the dynamical changes, (i.e. the fact the observations are non-contemporaneous) and inaccuracies in photometric trans-

Short Name	2MASS ID
Sources without infrared excess	
KPNO-Tau 4	J04272799+2612052
CFHT-Tau 15	J04274538+2357243
KPNO-Tau 5	J04294568+2630468
CFHT-Tau 16	J04302365+2359129
CFHT-Tau 13	J04312669+2703188
CFHT-Tau 7	J04321786+2422149
CFHT-Tau 5	J04325026+2422115
CFHT-Tau 11	J04350850+2311398
KPNO-Tau 9	J04355143+2249119
CFHT-Tau 2	J04361038+2259560
CFHT-Tau 3	J04363893+2258119
ITG 2	J04380083+2558572
Sources with infrared excess	
CFHT-Tau 9	J04242646+2649503
KPNO-Tau 6	J04300724+2608207
KPNO-Tau 7	J04305718+2556394
CFHT-Tau 12	J04330945+2246487
BDD399	J04381486+2611399
GM Tau	J04382134+2609137
CFHT-Tau 6	J04390396+2544264
CFHT-Tau 4	J04394748+2601407
CFHT-Tau 8	J04411078+2555116
BDD304	J04414825+2534304
BDD164	J04442713+2512164

Table 1. Table showing the short name used in this paper and the 2MASS ID from which the coordinates can be found. The division of sources with and without infrared excess is from Guieu et al. (2007).

formations. We note that although we have listed the uncertainties in Table 2 we adopt a Bayesian approach whereby the observations are precise and the uncertainties are a property of the model. This is equivalent to asking which underlying model, when combined with uncertainties representing our incomplete understanding of this model, will reproduce the precise observations. The construction of the uncertainties and how they are applied is described in detail in Appendix A.

3 THE MODELS AND FITTING

In order to model a combined star and disc system one requires a model of the stellar properties (luminosity, radius etc), the SED of the stellar photosphere and an initial model of the disc (structure, composition etc). The disc model is described as an initial model as some properties such as the vertical scale height or inner edge location may change (due to modelled physical processes) to some equilibrium state. Most existing studies of BDD systems involve parameterisation in order to remove the requirement for detailed physical modelling. For instance commonly made assumptions are that the central star emits as a black body, or as a naked photosphere without additional accretion flux. More subtly, one can simply pick a range of atmospheres at different effective (T_{eff}) temperatures, surface gravities ($\log(g)$) and bolometric luminosities (L_{bol}) to create a fitting grid, as opposed to using stellar interior models to derive these prop-

erties. Additionally, the inner edge and vertical structure of the disc can simply be prescribed analytically without inclusion of the detailed physics of magnetic truncation, dust sublimation and vertical hydrostatic equilibrium.

3.1 Dust Distribution

We have adopted a similar dust model to Wood et al. (2002) with the size distribution of dust particle given by

$$n(a)da = C_i a^{-q} \times \exp[-(a/a_c)^p] da \quad (1)$$

where $n(a)da$ is the number of particles of size a (within the interval da), a_c is the characteristic particle size, with p and q simply used to control the shape of the distribution. C_i controls the relative abundance of each constituent species (i) in the dust. We have adopted the following values for each parameter $q = 3.5$, $p = 0.6$ with $a_c = 50 \mu\text{m}$, also with an associated maximum and minimum grain size of $a_{\text{min}} = 5 \text{ nm}$ and $a_{\text{max}} = 1 \text{ mm}$. We set $C_i = 1$ and adjusted the species using a grain fractional abundance (an equivalent process to that of Wood et al. 2002), using the solar abundances of Asplund et al. (2006). The subsequent opacities are constructed from tabulated opacities for each species. More detail of the dust model can be found in Mayne & Harries (2010).

3.2 The Grids

In order to construct the stellar photosphere we interpolate the stellar interior models for a given age and mass and subsequently interpolate the stellar atmosphere models to the required T_{eff} , L_{bol} and $\log(g)$. This method is in contrast to the traditional method of selecting spectra over a range of T_{eff} , $\log(g)$ values and scaling the L_{bol} to match the observed fluxes at wavelengths shortward of the peak in disc emission ($\sim 3 \mu\text{m}$, Dullemond et al. 2001)¹. The accretion flux is then added, as prescribed in Mayne & Harries (2010), upon adoption of a rotation period (to derive the co-rotation radius). A disc component is then added and the radiative transfer through the system modelled to produce a simulated SED.

The modelling of the BDD systems was performed using the TORUS radiative transfer code. TORUS is detailed in Harries (2000) and was subsequently updated by Harries et al. (2004) and Kurosawa et al. (2004). TORUS uses the method of Lucy (1999) to solve radiative equilibrium on an AMR mesh. The code can also self-consistently solve the equation of vertical hydrostatic equilibrium and dust sublimation for the disc (Tannirkulam et al. 2007). The TORUS code has been extensively benchmarked (for radiative transfer in discs against Pinte et al. 2009). The addition of variable dust sublimation is described in Mayne & Harries (2010). We have constructed two grids using different assumptions about the properties and physics within the star disc system.

3.2.1 Ad-hoc Grid

The first model grid includes the effects of accretion. We place the inner edge of the gaseous and dust disc at the co-rotation radius and prescribed an initial analytical

¹ In effect this is a ‘by-eye’ pre-fitting to select an input stellar photosphere.

vertical disc structure. The initial disc structure is constructed using the analytical relationships (for the disc density and scaleheight) from Mayne & Harries (2010), $\rho = \rho_0 \frac{R_*}{r^\alpha} \exp(-\frac{1}{2}[z/h(r)]^2) \propto r^{-\alpha}$ and $h = h_0(r/R_*)^\beta$ where r and z are the radial and vertical cylindrical polar coordinates. The surface density (Σ) profile from these equations is $\Sigma(r) \propto r^{(\beta-\alpha)}$, and β and α are set such that $\Sigma(r) \propto r^{-1}$. This initial disc configuration follows the analytically prescribed disc structures of previous works, where SED fitting has been used to derive, for instance the β parameters or inner edge locations. These initial models are subsequently treated in one of two ways. Either, the vertical structure is fixed in the initial configuration and dust sublimation is modelled explicitly alongside a calculation of radiative equilibrium. Alternatively, hydrostatic equilibrium is enforced (via adjustment of the vertical structure and therefore β) in concert with the radiative equilibrium and dust sublimation calculations. This grid is termed the ad-hoc grid and is an extension of the grid featured in Mayne & Harries (2010). It covers only BD mass objects for the ages of 1 and 10 Myrs.

3.2.2 Semi-empirical Grid

The second grid is designed for non-accreting systems. In this case the inner edge is placed at the semi-empirically derived dust sublimation radius (only applicable for negligible accretion rates, see Whitney et al. 2004) and the vertical structure analytically prescribed, as for the ad-hoc grid. In this grid, the vertical structure and inner edge location do not change as dust sublimation and vertical hydrostatic equilibrium are not included. This grid is termed the semi-empirical grid and has an expanded mass and age range covering masses from 0.01 to 1.40 M_\odot and ages from 1 to 10 Myrs.

Note that our construction of the initial disc structures assumes that the dust is evenly distributed through the disc and follows the gas structure. We therefore implicitly exclude the possibility of dust settling in the disc for those models within the ad-hoc grid which enforce a hydrostatic structure on the gas distributions. However, the remaining models (i.e. a subset of the ad-hoc grid and all of the semi-empirical models) where the disc scaleheight structure is not required to fulfil hydrostatic equilibrium, can mimic the settling of the dusty component of the disc towards the mid-plane. Further complexity may be introduced by allowing the dust scaleheight to vary as a function of grain size (e.g. Tannirkulam et al. 2007, 2008) although we believe that additional observable constraints (such as scattered light imaging see Wood et al. 2002; Watson & Stapelfeldt 2007, for example) over and above SED fitting would be necessary to determine the degree of sedimentation. However, if dust settling or sedimentation is likely to be an important factor for a particular object then the semi-empirical grid or non-hydrostatic ad-hoc models are to be preferred. The details of which physical process are included in each grid are shown in Table 3².

² This information is also available online at <http://bd-server.astro.ex.ac.uk/calibration>.

3.2.3 Photometry

In most cases parameters are derived from photometric observations, either magnitudes or monochromatic fluxes, or conversions of the former to the latter. Therefore our SEDs need to be converted to apparent SEDs (via the application of a distance and extinction) and photometric observations simulated. We have simulated such photometric observations for a range of commonly used filter systems and the conversions, derivations of photometric measurements and definitions of the photometric systems are detailed in Appendix B. This information is important for observers who intend to use the fitting tool, as errors when adopting the incorrect photometric systems can be large (as mentioned in Section 2 and explained in Appendix A).

3.3 Fitting Statistic

As shown in Table 2 we have collected a large range of photometric observations in both magnitude and monochromatic flux systems. In order to perform a fit we must use consistent units and therefore we convert magnitudes to monochromatic fluxes. This conversion is performed in a rigorous manner by reversing the process described in Appendix B used to derive a simulated magnitude and then applying the process required to construct monochromatic fluxes (again described in Appendix B). This allows us to be confident that the models and data are being compared in a consistent manner.

Practically, fitting is performed by maximising the likelihood of the data being drawn from a given model. As the probability of the data being drawn from the i th model, P_m is

$$P_m = \prod_i e^{-\frac{(x_i - m_i)^2}{2\sigma_i^2}} \times \prod_j Q\left(\frac{x_j^u - m_j}{\sigma_j}\right), \quad (2)$$

where x_i and m_i are the i th data and model points (these are fluxes from the SED, monochromatic fluxes or magnitudes converted to fluxes), and σ_i the uncertainty of the i th data point. The second part of the equation derives the likelihood from the observed upper limits x_j^u is the j th upper limit with uncertainties σ_j , m_j the corresponding model flux and where Q is given by,

$$Q(x) = \frac{1}{2} - \frac{1}{2} \operatorname{erf}\left(\frac{x}{\sqrt{2}}\right), \quad (3)$$

where $\operatorname{erf}(x)$ is the error function. This in effect assumes that the σ is taken from a measurement of zero, but allows negative measured fluxes. Ideally, one would provide the measured flux and uncertainty as oppose to an upper limit, as this ensures the fitting routine does not have to make further assumptions about the data. In practice we choose to minimise the statistic $-2\ln(P_m)$, which as described in Naylor & Jeffries (2006) reduces to χ^2 for the case of data points with Gaussian uncertainties in one dimension (see also Cash 1979). In practice therefore we minimise the following statistic,

$$\chi_{\text{pseudo}}^2 = -2\ln\left(\prod_i e^{-\frac{(x_i - m_i)^2}{2\sigma_i^2}} \times \prod_j Q\left(\frac{x_j^u - m_j}{\sigma_j}\right)\right) \quad (4)$$

$$= \chi^2 + -2\ln\left(Q\left(\frac{x_j^u - m_j}{\sigma_j}\right)\right). \quad (5)$$

Grid Reference	ad-hoc Grid	semi-empirical Grid
Physical Processes		
Stellar Interior	Dusty-'00 ⁽¹⁾	$M_* \geq 0.02M_\odot$:BCAH98 ⁽²⁾ $M_* < 0.02M_\odot$: Dusty-'00 ⁽¹⁾ $T_{\text{eff}} < 1400$ K:AMES-Cond ⁽³⁾
Stellar Atmosphere	AMES-Dusty ⁽¹⁾	1400 K < T_{eff} < 2500 K:AMES-Dusty ⁽¹⁾ $T_{\text{eff}} > 2500$ K:NextGen ⁽⁴⁾
Accretion Luminosity	Yes	Yes-negligible
Vertical Structure	VHE Static	Static
Inner Dust Boundary	Variable Sublimation	Empirical Sublimation Radius
Inner Gas Boundary	Co-rotation Radius	Co-rotation Radius
Dust Scattering	Isotropic	Full Mie Phase Matrix
Parameters Covered		
Age (Gyrs)	0.001 & 0.01	0.001–0.01 ($\Delta=0.001$)
Mass (M_\odot)	0.01–0.08 ($\Delta=0.01$)	0.01–0.10 ($\Delta=0.01$), 0.10–1.40 ($\Delta=0.1$)
T_{eff}	Derived	Derived
$\log(g)$	Derived	Derived
Luminosity	Derived	Derived
Accretion Rate $\log \dot{M}$	–12– –6 ($\Delta=-1$)	–12
Areal Coverage (%)	1, 10	10
Disc Mass (M_*)		0.0, 0.01, 0.001
Disc Outer Radius (AU)	100, 300	50, 100
α (β^*)	Derived (VHE), 2.00 (1.00), 2.10 (1.10), 2.25 (1.25)	2.00 (1.00), 2.10 (1.10), 2.25 (1.25)
Scaleheight at 100AU (AU) ⁽²⁾	25	10
Inclination ($^\circ$)		0, 27, 39, 48, 56, 64, 71, 77, 84, 90
References. (1) Chabrier et al. (2000), (2) Baraffe et al. (1998), (3) Allard et al. (2000) and (4) Hauschildt et al. (1999)		

Table 3. Table describing the physical processes modelled in the two grids and the range of parameters the grids cover. (1) See explanation in Section 3. (2) this initial scaleheight is allowed to adjust if vertical hydrostatic equilibrium is enforced.

The online fitting tool then returns the N best fitting models to the user, with associated plots of χ^2_{pseudo} for each parameter. Uncertainties are derived using the 68% confidence interval by converting the given χ^2 values to a probability ($e^{-\frac{\chi^2_{\text{pseudo}}}{2}}$) and integrating from the most likely value until 68% of the total probability has been reached. Additionally, a Spearman’s rank correlation coefficient is derived for the best fitting 10% of models for each pair of free parameters, giving an indication of degeneracy. If two parameters are found to have evidence of degeneracy 2D χ^2_{pseudo} maps are created and presented alongside the fits, although this is only an indication of degeneracy.

The structure of the online fitting tools and comments on its use are detailed in Appendix B. Appendix B also includes details of the other tools available at <http://bd-server.astro.ex.ac.uk/> such as an SED browsing tool and isochrone server.

4 RESULTS

In traditional SED fitting values of extinction and distance are set to single values (i.e without uncertainties) for a given fit, allowing the number of free parameters to be reduced by two. However, this discards useful information as the distance and extinction uncertainties are well founded constraints. The depth (i.e. range of distances in a given population) of a given group of stars contributes little to shifts

within the HR-Diagram (Mayne et al. 2007; Mayne & Naylor 2008). However, when fitting monochromatic fluxes, or SED sections, to model SEDs variations in distance to individual objects can affect the flux significantly. For instance when fitting objects within Taurus the distance is usually set to 140 pc, or in some cases a modest distance uncertainty of ± 10 pc is used (Bertout et al. 1999). However, the distance range, from the most precise derivations of distances to three member stars, is 161 ± 0.9 , 147 and 130 pc, derived from interferometric observations (Torres et al. 2009). Therefore a more realistic distance range is 130–165 pc, which can lead to flux variations of up to a factor of 1.6. Assuming a distance of 140 pc for all objects in the Taurus region allows us to reduce the number of free parameters, but is less desirable than using a realistic range of distances. Uncertainties should also be adopted to apply to the extinction to each target object. The extinctions shown in Table 2 have all been sourced from Guieu et al. (2007) (for consistency), where they are adopted as single values (without uncertainty). These values, in turn, are derived in Guieu et al. (2006) where an uncertainty of ± 0.8 mags is quoted, which we have adopted. If we do not include such strongly physically motivated external constraints, like distance ranges, it is likely that, due to degeneracies of the parameters, the remaining free parameters will be optimistically constrained.

Figure 1 shows the infrared and near-infrared colour-magnitude (left panel) and colour-colour (right panel) diagrams (CMD & CoCoD) for targets from Table 2. A 1 Myr isochrone constructed using the interior models and atmo-

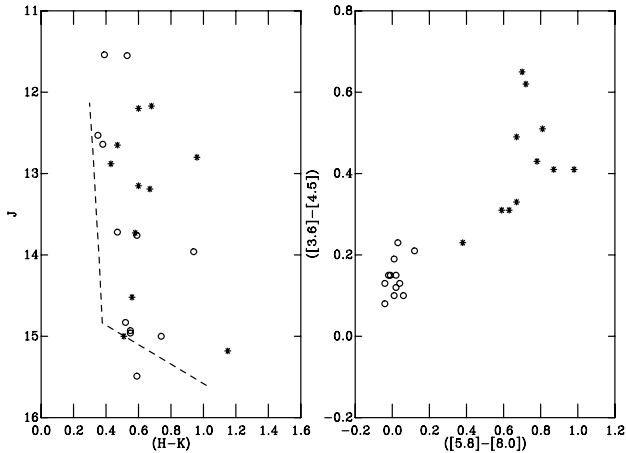


Figure 1. Figure showing the stars with (asterisks) and without (empty circles) infrared excesses from Table 2. The left panel shows a $J, H - K$ CMD and the right panel a $([3.6] - [4.5])$, $([5.8] - [8.0])$ CoCoD. The dashed line on the left panel shows an isochrone at 1 Myr for masses between 0.01 and $0.08 M_{\odot}$ adjusted to a distance of 140 pc and an extinction of $A_V = 1$.

spheric models of Chabrier et al. (2000) adjusted to a distance of 140 pc and an $A_V = 1$, is overlaid on the CMD (left panel).

The left panel of Figure 1 shows that the stars with (asterisks) and without (empty circles) discs lie redward and brighter than the illustrative isochrone. For the stars without discs several factors lead to a shift away from the model isochrone. Firstly, some objects lie behind extinction greater than the illustrative value selected (i.e. $A_V > 1.0$). Additionally, some stars without discs have luminosities above that predicted by the 1 Myr isochrone at a given colour or $H - K$ (for instance ITG 2, discussed in more detail in Section 4.2.1). Finally, some stars will also have a mass greater than the maximum mass included in the illustrative isochrone ($0.08 M_{\odot}$, for instance CFHT-Tau 5 also discussed in more detail in Section 4.2.1). Of course, for the stars with discs the same shifts will be present in addition to reddening of the system caused by the reprocessing of stellar light by the disc. As expected, the stars with infrared excesses are also clearly distinguishable in the right hand IRAC CoCoD, and the delineation agrees with the predicted values of $([3.6] - [4.5]) > +0.21$ and $([5.8] - [8.0]) > +0.13$ (Mayne & Harries 2010).

It is clear that the stars in Figure 1 do not lie along the isochrone, and therefore are poorly represented, in a CMD, by a simple coeval (naked photosphere) population at 1 Myr at a single distance and extinction with negligible accretion. The meaning and veracity of the inferred “age spreads” has been discussed at length in the literature (for a summary see Mayne & Naylor 2008). Several studies of classical T-Tauri stars (CTTS) have shown that active accretion and variations in distance cannot fully explain the spreads of stellar populations (Burningham et al. 2005; Da Rio et al. 2010). However, accretion, both past and current, has been identified as a major contributor to spreads in both luminosity and radii of young stars, and its effects on the magnitudes and colours of brown dwarfs with discs has been shown to be significant (Mayne & Harries 2010). Indeed Mayne &

Harries (2010) showed that the effects of accretion and disc presence on characterisation are more significant for lower mass systems.

A full discussion of the veracity of age spreads is beyond the scope of this paper. However, it is clear that fitting for an assumed coeval population can be performed by adopting a range of “isochronal ages”, whether they represent a stars true age or not. Additionally, a range of accretion rates and inclinations (leading to differing levels of occultation of the star by the disc) may be sufficient to provide the spreads observed, with the addition of a small intrinsic age spread which is less than the disc dissipation time (Littlefair et al. 2011; Jeffries et al. 2011).

4.1 Literature Stellar Parameters

For each of the objects within our sample we have attempted to find all the stellar parameters that authors have either derived or adopted for modelling and analysis of these objects. Table 4 presents, for each object, each value of the stellar parameter we have found, with the reference in superscript parenthesis (a legend is included in the table caption).

Table 4 does not contain information on how each quantity was derived (or indeed whether it was simply adopted), which is of course important. However, in cases where parameters were simply adopted in order to calculate or derive a dependent parameter it is still important to note the values of the input, which will, of course, determine the value of the derived property. For example Muzerolle et al. (2005) adopted approximate values for stellar parameters such as T_{eff} and mass, in order to model accretion and derive accretion rates for such objects, whereas, T_{eff} for these objects were derived from fitting to spectral type templates in Luhman (2004). Of particular note is that almost all of the stellar masses derived for these objects rely, in some way, on isochrones, which are known to be unreliable for low mass stars (see discussion in Mayne & Naylor 2008), under the assumption of coevality at an age of 1 Myr, and crucially, often at a set distance of 140 pc.

4.2 Naked Stars

The naked stars, which we assume are not accreting (supporting evidence is presented in Table 7 discussed in Section 4.4.1), were fit using the semi-empirical grid to allow a range of isochronal ages as observed in the CMD, Figure 1³. There is no difference, except the accretion luminosity, between the naked photospheres used in the ad-hoc and semi-empirical grids, although the latter includes a wider range of ages and masses⁴.

Figure 2 shows an example of a fit to CFHT-Tau 16 using the semi-empirical grid of models and the observations presented in Table 2. We have fitted this star in three different ways. Firstly, we have fitted the star allowing all of the

³ We note that these values should not be adopted as the real ages of the system. As discussed in Section 4 ages derived from isochrones are currently inaccurate for LMS and BDs.

⁴ Of course, the models of systems at higher masses will include stellar atmospheres and interiors appropriate for the higher T_{eff} values.

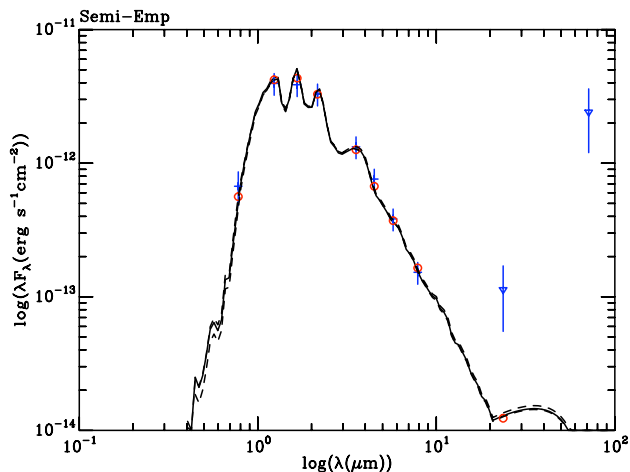


Figure 2. SEDs of the best fitting models from semi-empirical grid, showing fits to the entire grid (dashed green line), using a set distance and extinction (dashed black line) and a restricted grid (solid black line). The monochromatic fluxes derived from the best fitting model from the restricted grid are shown as red circles and the observations as blue crosses (fluxes) or triangles (upper limits) with uncertainties shown as bars. Note, the fits for this object are closely matched and therefore the resulting SEDs show little deviation, meaning the lines for each fit are essentially over plotted and some may not be visible.

parameters of the model grid to be free. Secondly, we have fitted the star by setting the distance to 140 pc and extinction to the single values from Table 2 (following Guieu et al. 2007). Finally, we have performed a fit using observations, shown in Table 4 to constrain the model grid parameters alongside distance and extinction uncertainties. In the case of CFHT-Tau 16, all of the fits yielded similar results. The resulting χ^2 parameter space for the case where the parameters are all free is shown in Figure 3.

Figure 2 shows that in the case of CFHT-Tau 16 the best fitting SEDs, for each fit type, are well matched. This is reflected in the consistency of the derived parameters, for this object, shown in Table 5 (described later). However, Figure 3 shows that even in this excellent case some parameters remain formally unconstrained when the confidence intervals are examined. The 68% confidence intervals for the extinction and mass parameters are within the fitted parameter space, but the distance upper bound is unconstrained. The distance ranges selected, however, are strongly constrained by the range of distances found to existing members and should not be extended. It is usually inadvisable for an object to be fitted to the entire grid, since degeneracies in the parameter space can lead to derivations of incorrect parameters. For instance the effects of increasing mass, decreasing distance and increasing accretion rate all act to increase the luminosity of the system and therefore can lead to compensating errors, especially when combined with adjustments in extinctions. This is especially significant for lower temperature stars as the region of the SED sensitive to stellar and disc properties overlap (Clarke & Pringle 2006). Indeed Mayne & Harries (2010) show that a population of accreting BDD systems can appear both spectroscopically and photometrically similar to a population of CTTS under heavy extinction and at a different distance.

For the remaining sample of naked BDs we have fitted using the final two methods applied to CFHT-Tau 16, i.e. fitting using a set distance and extinction, and fitting using a restricted grid with all parameters constrained by observations (in other words we do not fit using a grid where all the parameters are free). Figure 4 shows the best fitting SEDs for each of the naked objects. The solid and dashed lines show the fits allowing distance and extinction to vary over the prescribed ranges and setting them to fixed values, respectively. The model fluxes, for the restricted case, are shown as circles and the observations as crosses, with triangles denoting upper limits.

The parameters derived for the restricted fitting grid are shown in Table 5. Table 5 shows the best fitting values for the independent variables with 68% confidence intervals and the dependent variables associated with the best fitting model. Some of the confidence intervals indicate a 0.0 increment in either direction, this is sometimes caused by the best fitting value reaching a boundary (for example 165 pc in the range 130–165 pc as is the case for CFHT-Tau 16). This may indicate that the parameter is poorly constrained, however, as the boundaries for the fitting grid have been chosen using external literature constraints this is not necessarily a problem.

Comparison between the values derived in Table 5 and the literature values (Table 4) show reasonable agreement. For most objects our derived masses match, within the uncertainties, those found in the literature and the effective temperatures match to within ~ 100 K, with the exception of ITG 2, CFHT-Tau 5 (which are discussed in Section 4.2.1) and KPNO-Tau 4. For KPNO-Tau 4 the discrepancy in the effective temperatures is large with a difference of ~ 350 K. This is most likely caused by this object existing at the boundary in our grid between the AMES-Dusty (Chabrier et al. 2000) and AMES-Cond (Allard et al. 2000) models, which as shown in Mayne & Harries (2010) leads to a significant discontinuity in photometric magnitudes.

For most cases allowing the distance to change over the observed range, and adding an uncertainty to the extinction, results in parameters which are consistent (within the uncertainties) with those derived with a set distance and extinction (excepting ITG 2 and CFHT-Tau 5). However, the best fitting values are often slightly different, meaning the derived dependent variables do vary. For example changes in the T_{eff} are, for the most extreme cases of CFHT-Tau 11 and KPNO-Tau 9, 134 or 289 K respectively, however for the remaining fits they are below 100 K.

4.2.1 Problem Fits

We were unable to achieve acceptable fits using a restricted parameter space, to the objects ITG 2 and CFHT-Tau 5. For ITG 2 setting the distance and extinction and allowing the rest of the grid parameters to run free also resulted in a poor best fit model. For CFHT-Tau 5, however, an acceptable fit was found using a set distance and extinction but allowing the stellar mass to increase significantly. To explore the problems with these objects we have also fitted them using the entire grid. The resulting best fits are presented in Figures 5 and 6, alongside those already presented in Figure 4. For ITG 2 the only way we could derive a best fitting SED close to the observed data points was to allow the mass of

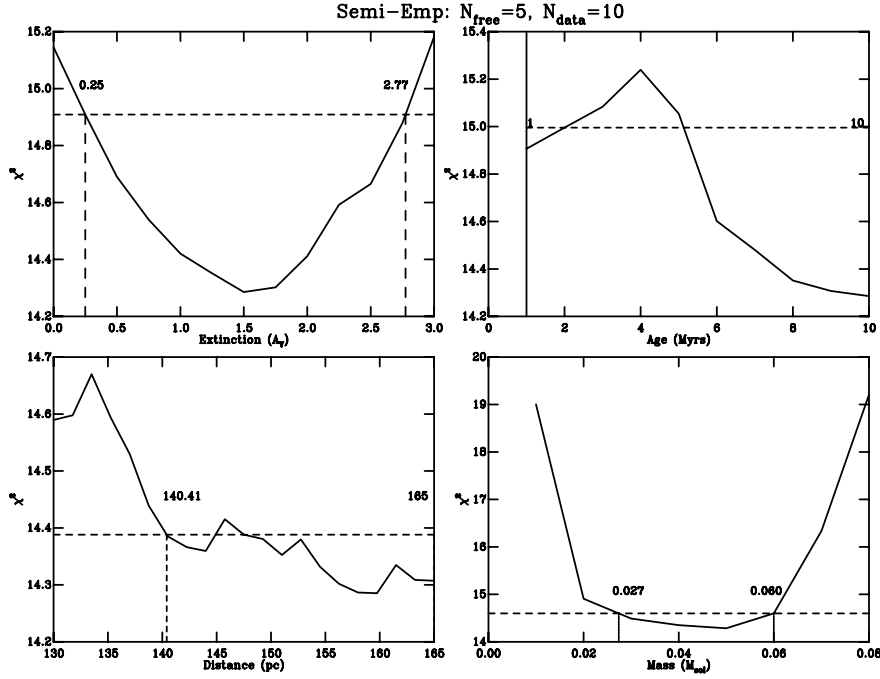


Figure 3. Figure showing the χ^2 distributions for the fit to the whole semi-empirical grid for CFHT-Tau 16, where the dashed lines show the 68% confidence limits. For each plot the remaining parameters have been held at their best fitting values.

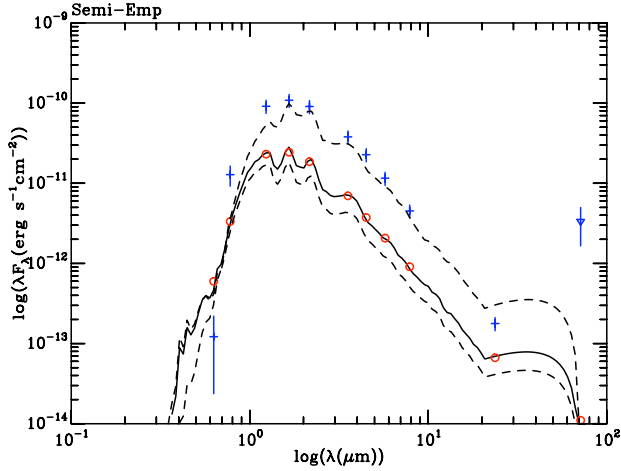


Figure 5. SEDs and monochromatic fluxes for ITG 2 where symbols have the same meanings as Figure 2.

the star (M_*) to increase to $0.2 M_\odot$ and allow the extinction and distance to increase to $\sim 5 A_V$ and 165 pc respectively. The resulting star has a much higher effective temperature of 3193 K , $\log(g)$ of 3.40 , radius of $1.45 R_\odot$ and a luminosity of $\log(L/L_\odot) = -0.700$. These values are inconsistent with the literature properties presented in Table 4. For CFHT-Tau 5 the best fitting SED returned values of, $M_* = 0.1 M_\odot$, distance = 140.50 pc , $A_V = 0.50$, $\log(L/L_\odot) = -1.160$, $T_{\text{eff}} = 3002$, $\log(g) = 3.45$ and a radius of $0.968 R_\odot$. Again, as with ITG 2, these parameters are inconsistent with the literature values presented in Table 4.

These objects are at much higher luminosities, for their

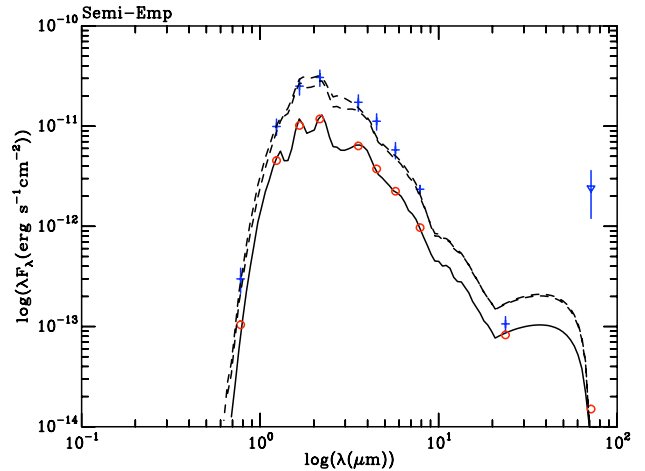


Figure 6. SEDs and monochromatic fluxes for CFHT-Tau 5 where symbols have the same meanings as Figure 2.

given masses, than the youngest (i.e. 1 Myr) isochrone. This means that these stars are poorly fit by both of our grids. Hence, we can only achieve these luminosities by increasing the stellar mass and compensating for the SED shape by increasing the extinction. Table 4 shows that CFHT-Tau 5 has a similar luminosity to CFHT-Tau 7, however, the latter object has a significantly higher mass and is, therefore, not affected by this problem. This limitation means that for very, “isochronally” young stars we will be unable to reproduce their SEDs with our current grid. We are currently running a grid of models which are divorced from isochronal theory and will extend to this region of parameter space (explained

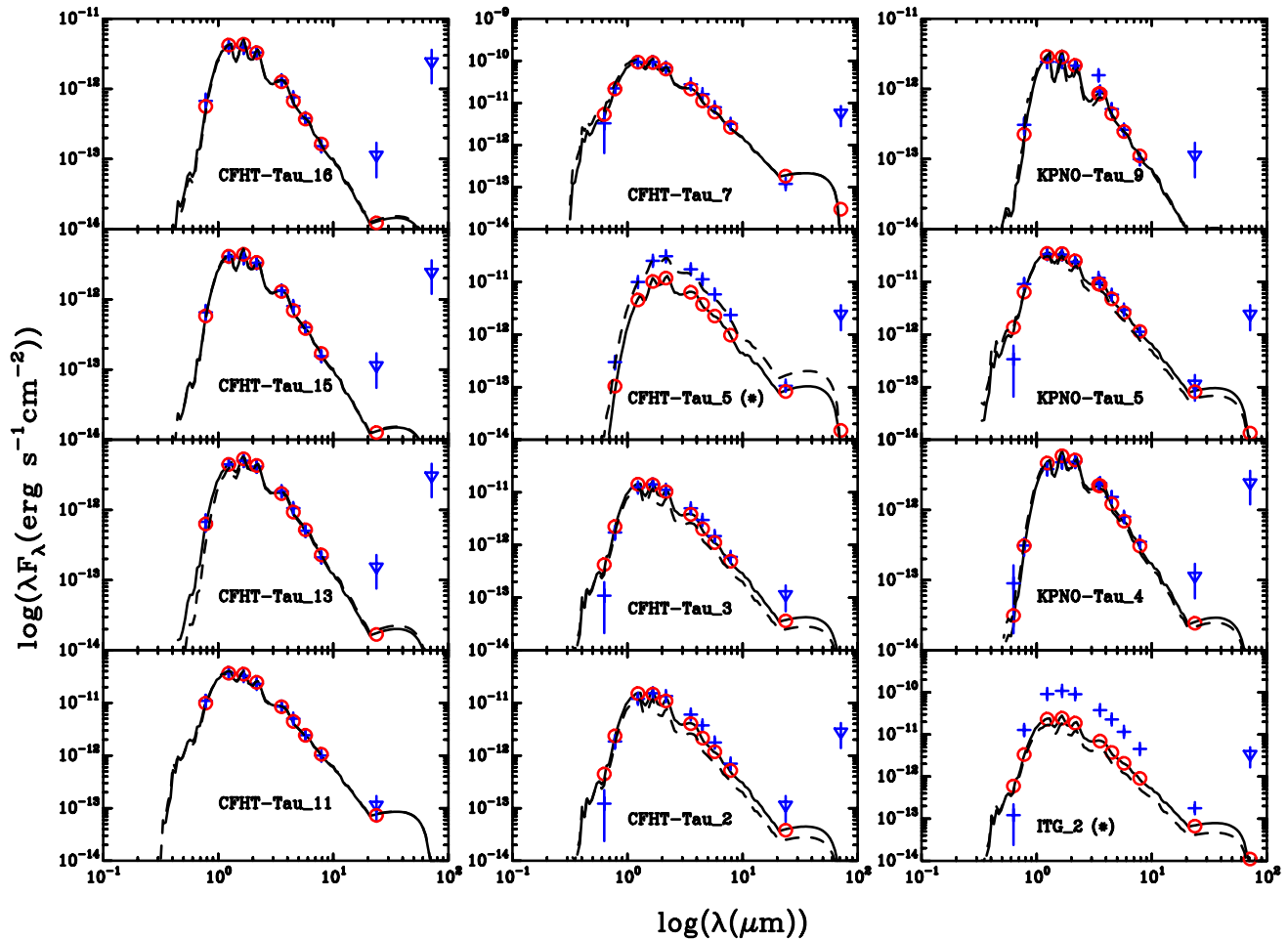


Figure 4. The best fitting SEDs for the naked objects, all from the semi-empirical grid. The solid black lines are the SEDs from the restricted fits and dashed lines show the best fitting SEDs when the distance and extinction have been set. The monochromatic fluxes derived for the best fitting restricted model are shown as circles and the observed fluxes, (from Table 2) are shown as crosses, or triangles for upper limits, with the bars denoting the uncertainties. It can be seen that we failed to find a satisfactory fit for ITG 2 and CFHT-Tau 5 denoted by (*).

in more detail in Section 6). It is interesting to note that the SEDs of such objects cannot be reproduced if we allow the accretion rates to increase, even though they are naked stars (some supposed naked stars have been found with non-negligible accretion rates Kennedy & Kenyon 2009, these are discussed in Section 4.4.1). The accretion diagnostics for the sample have been collected (Table 7) and are discussed later in Section 4.4.1.

4.3 Stars with Discs

For the BDD objects we have fitted to the ad-hoc grid to allow for a range of accretion rates, again using either a set distance and extinction or the restricted grid with varying distance and extinction. One important note is that, as discussed in Section 3.2.1, the observed dust disc structures may not appear in hydrostatic equilibrium due to grain settling. Therefore, we have included the ad-hoc models with pre-

scribed disc structures in the fitting process. This may also be a reason to favour the semi-empirical models for systems with significant grain settling, but with negligible accretion rates.

Figure 7 shows the best fitting SEDs for the BDD objects from the ad-hoc grid. As for Figure 4 the solid and dashed lines show the fits allowing distance and extinction to vary over the prescribed ranges (the restricted fits) and those with distance and extinction set at fixed values, respectively. The model fluxes, for the restricted case, are shown as circles and the observations as crosses, with triangles denoting upper limits.

Figure 7 shows that the fits do not change significantly upon fixing the distance and extinction, with the exception of CFHT-Tau 8. It is clear that all observations are well fit with accreting 1 Myr disc structures drawn from the ad-hoc grid, again excepting CFHT-Tau 12. The best fitting param-

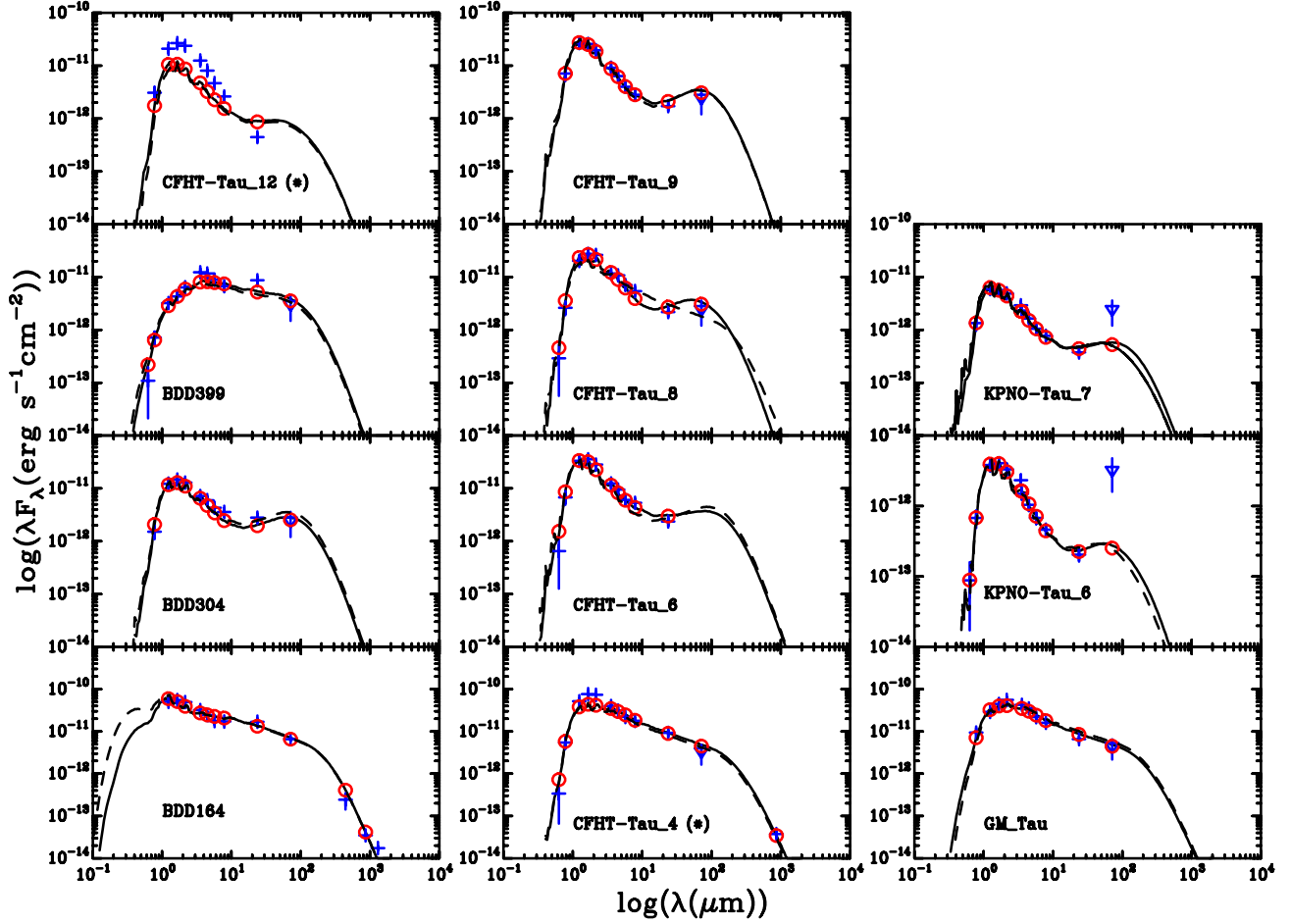


Figure 7. The best fitting SEDs for the BDD objects, from the ad-hoc grid. The solid black lines are the SEDs from the restricted fits and dashed lines show the best fitting SEDs when the distance and extinction are fixed. The monochromatic fluxes derived for the best fitting restricted model are shown as circles and the observed fluxes, from Table 2, are shown as crosses, or triangles for upper limits, with the bars denoting the uncertainties. It can be seen that we failed to find a satisfactory fit CFHT-Tau 12 and, to a lesser extent, CFHT-Tau 4, which are denoted by (*).

eters derived for the BDD systems using a restricted grid drawn from the ad-hoc model grid are presented in Table 6

We found that fixing the distance and extinction only affects the derived best fit parameters significantly in a few examples when using the ad-hoc grid. For example, the best fitting mass for BDD304 increases by $0.02M_{\odot}$ when the distance and extinction are set. For most objects the derived accretion rates are consistent with those found in previous studies (see Table 7). Additionally, in all cases except CFHT-Tau 12 and CFHT-Tau 9 the parameters derived for the targets using the accretion models (i.e. ad-hoc) are consistent with the spread of values presented in Table 4. It is clear from Table 6 that we are unable to differentiate between accretion rates ranging from $\log \dot{M} = -12$ to -9 . This is due to unavailability, or poor quality of, optical photometry which covers the shorter wavelength range where accretion flux is the dominant contributor to the SED. The derived accretion rates are discussed in detail in Section 4.4.1.

We also fitted the BDD objects to the semi-empirical grid, where accretion rates are negligible but a larger range of ages and masses is available. For all BDDs, excepting BDD399, BDD304, BDD164 and CFHT-Tau 4, acceptable fits could be found using the non-accreting models. This is as the effects of a disc and accretion on observations of a BDD system can mimic a star of higher mass or younger age (Mayne & Harries 2010). Therefore observations of systems with discs, can be fit using SEDs of accreting and non-accreting models. For instance for CFHT-Tau 8 and KPNO-Tau 6 best fitting masses of 0.1 and $0.05 M_{\odot}$ (and ages of 5 Myrs) were found with the semi-empirical grid, compared to 0.08 and 0.03 found using the ad-hoc grid, and 0.078 and $\sim 0.025 M_{\odot}$ (for an age of 1 Myr) found in the literature (see Table 4). It is perhaps surprising that even in these cases, where a large range of photometric measurements are used, that there can still be some confusion as to whether a source is accreting, or if it is in fact a more massive and younger ob-

ject. This suggests, as detailed in Mayne & Harries (2010) that selection of stars from CMDs and subsequent investigation into their mass and accretion rate relationship is unreliable. In the case of CFHT-Tau 12 the fit is actually better when using the semi-empirical grid, however several models cannot be fit without allowing for accretion flux, i.e. BDD399, BDD304, BDD164, GM Tau and to a lesser extent CFHT-Tau 4.

4.4 Derived Parameters

The main differences between our models of BDD systems and those used in previous studies is the additional modelling of accretion luminosity, vertical hydrostatic equilibrium and dust sublimation. The main derived parameters which indicate the veracity of these mechanisms, when compared to observations, are the accretion rate, inner edge location and flaring parameter. Without the inclusion of these physical mechanisms it is clear from previous works and from the fits in this paper that reasonable fits can still be achieved and parameters derived. However, if important physical processes are neglected it is questionable whether these parameters are reliable and whether we are learning anything about the physical mechanisms governing these systems.

4.4.1 Accretion

Accretion rates of $\log \dot{M} < -9$ contribute little to shifts within the HR-Diagram (Mayne & Harries 2010). However, when fitting monochromatic fluxes or SED sections to model SEDs variations in accretion rate below this threshold can affect the flux significantly (Mayne & Harries 2010). This can apply to objects with and without discs e.g. Kennedy & Kenyon (2009) find 43 stars in their sample of 1253 are actively accreting whilst no disc is detected.

The adopted magnitudes (from Table 2) do not extend across the optical regime, i.e. magnitudes at U, B and V. This does mean that a large section of the SED remains unconstrained. Fitting has been performed by adopting magnitudes or deriving fluxes from photographic plate observations, such as the NOMAD catalogue (Zacharias et al. 2005) by Bouy et al. (2008). However, the spectral responses of the photographic plates are poorly constrained and therefore subsequent transformation to another photometric system or to a monochromatic flux are unreliable (see Appendix B2). However, as accretion flux can contribute significantly in the optical regime allowing this parameter to run free may lead to best fitting models having elevated or unrealistic levels of accretion. Therefore, we have collected photometry from Zacharias et al. (2005) for as many of our objects as possible alongside H_α equivalent widths and derived accretion rates, which are presented in Table 7. As many of our objects cannot be satisfactorily fit without accretion flux these values can be used to support their status as active accretors. These values can only be used as a guide to add support for an accreting or non-accreting model. The optical photometry is quite unreliable and it is very difficult to compare measured widths of H_α made with different instruments or over different epochs due to their variability (Jayawardhana et al. 2006), so one cannot use these values as strong constraint.

Table 7 shows accretion diagnostics in the form of H_α equivalent widths for our targets as found by various authors, and derived accretion rates for some objects. Table 7 also shows our derived accretion rates for the BDD objects.

We have assumed negligible accretion rates for all of the BD systems and Table 7 shows that this is a good assumption for these objects. For the BDD objects, in most cases, our accretion rates are consistent with those derived in the literature. Alternatively, where we have derived non-negligible accretion rates the EW(H_α) and blue photometry support this. Several individual cases, however, will be investigated further in Section 4.4.3.

4.4.2 Disc Structure

The ad-hoc grid includes a state-of-the-art treatment of dust sublimation and vertical hydrostatic equilibrium. Therefore, one would expect to find significant differences between the inner edge locations, inclinations and flaring parameters derived in this work, and those derived by studies using an analytical or semi-empirical approach (for instance placing the inner edge at a predefined sublimation radius).

Table 8 shows our best fitting inclinations, inner edge locations (converted to AU) and $\beta(1-\alpha)$, the flaring parameter) compared against those derived in Guieu et al. (2007) for the BDD targets, where available⁵. The disc structures and surface density profiles are varied in Guieu et al. (2007) but the corresponding value of the surface density exponent of the best fitting model is not published, so comparisons in Table 8 are incomplete. Our best fitting total disc masses are presented in Table 6 for each of the BDD systems. Whereas the models used in Guieu et al. (2007) adopted a single disc mass of $1 M_J$.

Table 8 shows that, in general, our inner edge locations, or more precisely the position of our dust sublimation radii, are often much closer to the star than those found in Guieu et al. (2007). This is caused by the inclusion of accretion flux in our models and realistic dust sublimation as opposed to the prescription of a vertical wall. As discussed in Mayne & Harries (2010) the resulting inner edge structures are curved, consistent with detailed studies (Tannirkulam et al. 2007) of the inner edges of circumstellar discs, which leads to significant changes in the way the SED around 1–10 μm changes with inclination. This means we are able to achieve fits aesthetically similar to those of Guieu et al. (2007) but with significantly different inner edge locations. It is however difficult to perform a complete comparison as Guieu et al. (2007) do not publish their best fitting inclinations. Additionally, Guieu et al. (2007) only model inner edge positions of 0.015–0.3 AU from the central star, which does not extend low enough to match some of our models.

4.4.3 Specific Cases

Further comparison and investigation into the structures of the discs can be performed in a few cases where either, the fitting process has revealed interesting results or further studies have been performed on the object in question.

⁵ Guieu et al. (2007) do not publish their best fitting inclinations or the fits for CFHT-Tau 12 and BDD399

Name	Equivalent Width of H α (\AA)	$\log \dot{M}$	B_{plate}	V_{plate}	$\log \dot{M}^*$
Sources without infrared excess					
CFHT-Tau 16	-16.76 ⁽¹⁾				<-12
CFHT-Tau 15	-18.90 ⁽¹⁾				<-12
CFHT-Tau 13	-3.60 ⁽¹⁾				<-12
CFHT-Tau 11	-45.07 ⁽¹⁾		20.31	17.97	<-12
CFHT-Tau 7*	-8.63 ⁽¹⁾ , 5.5 ⁽⁸⁾		18.83	17.96	<-12
CFHT-Tau 5	-29.84 ⁽¹⁾				<-12
CFHT-Tau 3	-10.5 ⁽⁴⁾ , 50 \pm 4 or 65 \pm 1 ⁽³⁾ , -55 \pm 4 ⁽⁷⁾	<-12 ⁽⁴⁾			<-12
CFHT-Tau 2	11 \pm 1 ⁽³⁾ , -13 \pm 4 ⁽⁷⁾		20.70		<-12
KPNO-Tau 9	20 ⁽²⁾				<-12
KPNO-Tau 5	30 ⁽³⁾		20.56		<-12
KPNO-Tau 4	150 ⁽²⁾ , -38.4 ⁽⁴⁾ -158.08 ⁽¹⁾	<-12 ⁽⁴⁾			<-12
ITG 2					
Sources with infrared excess					
CFHT-Tau 12	-79.4 ⁽¹⁾				-12 ^{+3.00} _{-0.00}
BDD399	-47 ⁽⁴⁾	-10.8 ⁽⁴⁾			-8 ^{+0.07} _{-1.00}
BDD304	-233.7 ⁽⁴⁾	-11.3 ⁽⁴⁾	20.33		-9 ^{+1.03} _{-1.00}
BDD164		-11.03 ⁽⁴⁾ , -9.7 ⁽⁹⁾	19.27	17.89	-8 ^{+0.55} _{-3.34}
CFHT-Tau 9	-9.95 ⁽¹⁾		20.59		-9 ^{+0.13} _{-3.00}
CFHT-Tau 8	-52 ⁽¹⁾				-10 ^{+1.03} _{-1.00}
CFHT-Tau 6	-102 ⁽⁴⁾ , -63.7 ⁽¹⁾	-11.3 ⁽⁴⁾	19.99		-9 ^{+0.06} _{-3.00}
CFHT-Tau 4	-129.3 ⁽⁴⁾ , 69 \pm 4 ⁽³⁾	-11.3 ⁽⁴⁾			-9 ^{+0.14} _{-3.00}
GM Tau		-8.7 ⁽⁶⁾	18.39	17.45	-8 ^{+0.63} _{-3.11}
KPNO-Tau 6	350 ^(2,3) , -207.91 ⁽¹⁾ , -41.1 ⁽³⁾	-11.4 ^(4,5)			-10 ^{+0.05} _{-2.00}
KPNO-Tau 7	300 ^(2,3) , -31.1 ⁽⁴⁾	-11.4 ⁽⁴⁾			-10 ^{+0.90} _{-2.00}

Table 7. Table of accretion indicators for sources with and without infrared excesses as defined in Guieu et al. (2007). (*) the $\log \dot{M}$ in column 6 is from this work. References: (1) Guieu et al. (2006), (2) Briceño et al. (2002), (3) Jayawardhana et al. (2003), (4) Muzerolle et al. (2005), (5) Herczeg & Hillenbrand (2008), (6) White & Basri (2003), (7) Martín et al. (2001), (8) Kraus & Hillenbrand (2009) and Bouy et al. (2008). B_{plate} and V_{plate} photometry is from Zacharias et al. (2005).

CFHT-Tau 12 is better fit using a semi-empirical model with a negligible accretion rate, rather than an accreting model from the ad-hoc grid. Figure 8 shows the fits for CFHT-Tau 12 using both grids. Figure 8 shows that the semi-empirical grid yields a much better fitting SED in all cases. Most parameters, and their uncertainties, are consistent between the fits in the two grids. However, the best fitting mass is marginally increased, the distance and inclination decreased, and the age moves from 1 Myr to 2 Myrs. Only by allowing the accretion rate to move to $\log \dot{M} = -7$ can we get an acceptable fit using the accreting, ad-hoc models (dashed green line left panel, Figure 8). Such an extreme accretion rate is unlikely but there is little additional information in Table 7 to constrain this, other than a non-contemporaneous H α equivalent width measurement. It is interesting to note that CFHT-Tau 12 has no measurements at wavelengths longer than 24 μm (see Table 2) leading to poor constraint of the cooler dust disc at larger radii, however our best fitting disc mass is $M_{\text{disc}} = 0.001 M_*$, with no acceptable fit to an $0.01 M_*$ disc model found.

BDD399, BDD164, BDD304, GM Tau and CFHT-Tau 4 are all poorly fit when using the semi-empirical grid, (i.e. assuming negligible accretion and allowing age to vary). This is not unsurprising as for each of these objects there is evidence of non-negligible accretion rates, as shown in Table 7. If such objects are fitted without accretion luminosity

the mass of the central star is increased and its distance decreased, to increase the short-wavelength luminosity.

Figures 9, 10, 11, 12 and 13 show the fits from both grids (semi-empirical and ad-hoc) for all fit types (i.e. using the entire grids, refining the fit and finally setting only the distance and extinction).

For BDD399 fitting to the entire semi-empirical grid, still does not result in a satisfactory fit. As stated in Luhman et al. (2007) the photosphere is too faint for any model of a young BD. However, as we can see in the left panel of Figure 9 the fit is much more consistent for all fit types in the ad-hoc grid, and indeed yields similar parameters. The derived accretion rate for this object is $\log \dot{M} = -8^{+0.07}_{-1.00}$ (for the restricted fit) which is greater than the literature result of -10.8 (Muzerolle et al. 2005). This object was studied in detail in Luhman et al. (2007) where an inclination of 70 $^\circ$ was found with an inner disc radius of 58 R_* and outer radius of $R = 20\text{--}40$ AU. The central star of Luhman et al. (2007) had a luminosity of $-1.2218 \log \left(\frac{L_*}{L_\odot} \right)$, a mass of $0.05 M_\odot$ and a radius of $1.02 R_\odot$. We find an inclination angle of 64 $^\circ$, an inner disc radius of 6.4 R_* and an outer disc radius of 100 AU, with a corresponding star of luminosity $-1.3400 \log \left(\frac{L_*}{L_\odot} \right)$ mass of $0.08 M_\odot$ and radius $0.829 R_\odot$. We derived a best fitting disc mass for this object of $M_{\text{disc}} = 0.001 M_*$. Whilst our inclinations are consistent with that of Luhman et al. (2007) our fit is hampered by the fact that the luminos-

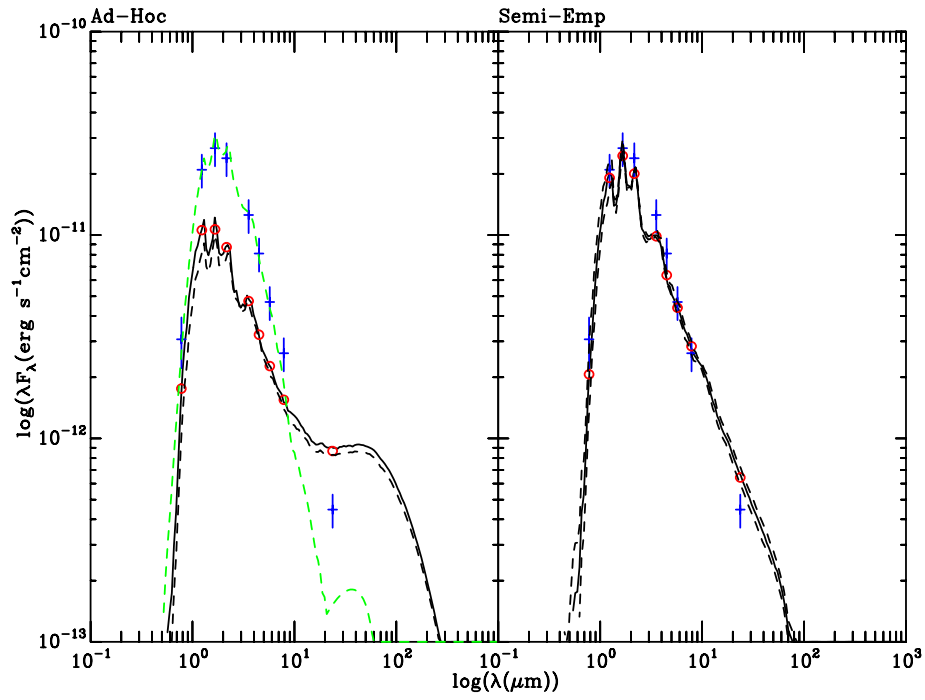


Figure 8. SEDs and monochromatic fluxes for CFHT-Tau 12 where symbols have the same meanings as Figure 2.

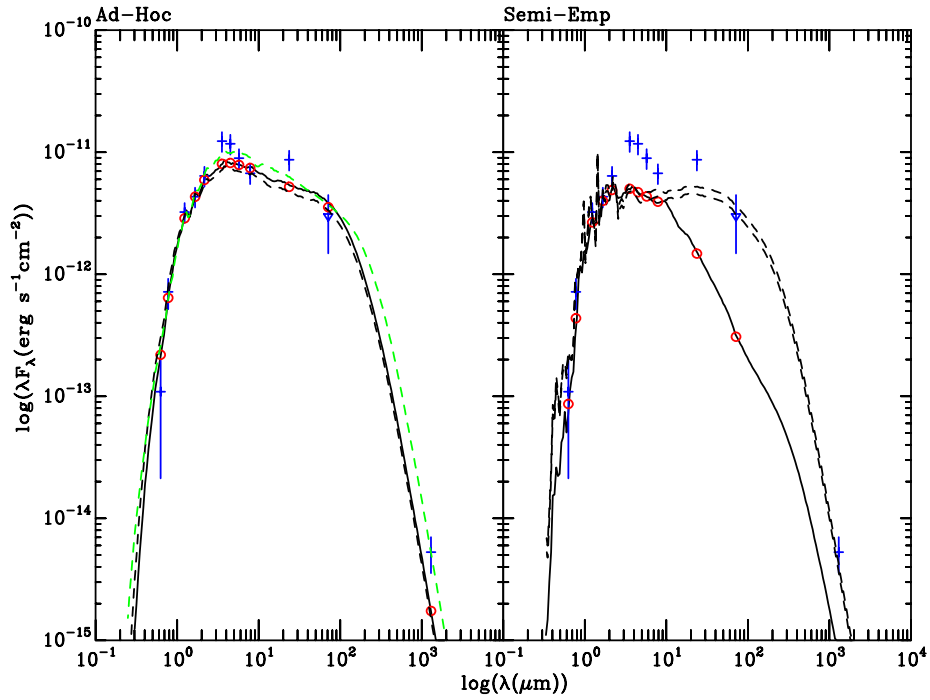


Figure 9. SEDs and monochromatic fluxes for BDD399 where symbols have the same meanings as Figure 2.

Name	Source	Inclination ($^{\circ}$)	β ($0=VHE$) ⁽¹⁾	R_{sub} (AU) ⁽²⁾
Sources with infrared excess				
CFHT-Tau 9	This paper	$64^{+2.49}_{-37}$	0 (1.25)	0.0081
	Guieu et al. (2007)		1.125	0.032–0.067
KPNO-Tau 6	This paper	$64^{+5.22}_{-37}$	0 (1.25)	0.0036
	Guieu et al. (2007)		1.0–1.125	0.032
KPNO-Tau 7	This paper	$71^{+0.99}_{-71}$	1.25 (0)	0.0043
	Guieu et al. (2007)		1.0–1.125	0.015
CFHT-Tau 12(*)	This paper	$64^{+5.87}_{-16}$	1.25 (0)	0.0058
	Guieu et al. (2007)		Not Published	
BDD399	This paper	$64^{+0.00}_{-0}$	1.10	0.025
	Guieu et al. (2007)		Not Published	
GM Tau	This paper	$48^{+8.01}_{-9}$	1.10	0.025
	Guieu et al. (2007)		1.0	0.015–0.067
CFHT-Tau 6	This paper	$48^{+8.66}_{-21}$	1.25 (0)	0.064
	Guieu et al. (2007)		1.0–1.125	0.067–0.14
CFHT-Tau 4	This paper	$39^{+9.44}_{-12}$	1.10	0.025
	Guieu et al. (2007)		1.0	0.14–0.3
CFHT-Tau 8	This paper	$71^{+0.76}_{-49.43}$	0 (1.25)	0.025
	Guieu et al. (2007)		1.0–1.125	0.015–0.067
BDD304	This paper	$71^{+2.17}_{-71}$	1.25 (0)	0.022
	Guieu et al. (2007)		1.125	0.015–0.032
BDD164	This paper	0^{+56}_{-0}	1.10	0.025
	(Guieu et al. 2007)		1.125	0.032–0.067

Table 8. Table of disc structure parameters for sources with infrared excesses as defined in Guieu et al. (2007). Here our R_{sub} radii have been converted to AU and a β parameter constructed using $1 - \alpha$ (see Section 3). Inclinations from our work are included but inclinations are not published in Guieu et al. (2007). (1) As the β variables can take only four values uncertainties are meaningless we simply quote the best fitting values and if models with the alternate value were found to have χ^2 values within the 68% confidence interval their values are quoted in brackets. (2) the R_{sub} from our work is positioned according to the balance of stellar flux and disc temperature, the range chosen in Guieu et al. (2007) is 0.015–0.3 AU.

ity of the stellar photosphere of BDD399 is under-luminous when compared to isochronal models (a grid is in preparation to improve on this limitation). As Luhman et al. (2007) obtained images of the disc directly their derived disc parameters should be viewed as more reliable.

For BDD164 a satisfactory fit can only be achieved with an accreting model, however in this case our derived accretion rate of $\log \dot{M} = -8^{+0.55}_{-3.34}$ is consistent with the values of -11.03 and -9.7 (Muzerolle et al. 2005; Bouy et al. 2008), albeit with the best fitting rate elevated over the literature values again. Bouy et al. (2008) studied this object in detail using multi-wavelength photometry (although as noted in Section 4.4.1 they used NOMAD photometry in the optical regime which is derived using photographic plates in this case). They found the best fit for a disc with inner radius at 0.04 AU and a β value of 1.1 or 1.2 (consistent with an α of 2.10 or 2.20 in this work) for a central star with mass $0.045M_{\odot}$. We find an α of 2.10 and an inner disc radius of 0.025 AU for a star with mass $0.07\text{--}0.08M_{\odot}$, with a best fitting total disc mass of $M_{\text{disc}}=0.01M_{*}$.

For BDD304, Figure 11 again reveals a requirement of an accretion flux when this object is fitted and comparison of the derived parameters from Tables 6 and 7 shows that we

derive an elevated accretion rate, $\log \dot{M} = -9^{+1.03}_{-1.00}$, compared to -11.3 (Muzerolle et al. 2005). We find a best fitting disc mass of $M_{\text{disc}}=0.001M_{*}$ for this object.

For GM Tau, even using the accreting models of the ad-hoc grid we are unable to achieve a completely satisfactory fit, as shown in Figure 12. This is caused by the fact that the mass of GM Tau is estimated to be at or above the higher mass boundary of the ad-hoc grid ($M_{*} = 0.08M_{\odot}$, compared to 0.078, see Table 4). Indeed, this can be seen when fitting using the semi-empirical grid where the mass derived is much higher. It is interesting to note that if the monochromatic fluxes were fitted to the entire grid (only setting the distance and extinction), as shown in Figure 12 a satisfactory fit can be obtained whereby the object looks very similar to a higher mass object at higher inclinations, $M_{*}=0.8M_{\odot}$ at 64° (as highlighted by Mayne & Harries 2010). This highlights the problems of using fitting tools such as the one featured in this paper and that of Robitaille et al. (2006) without pre-selecting, or refining the parameter space (this point is also emphasised in Robitaille et al. 2006). The best fitting disc mass derived for this object was $M_{\text{disc}}=0.01M_{*}$.

As with GM Tau for CFHT-Tau 4 we cannot achieve a fit comparable to the other objects in our sample using

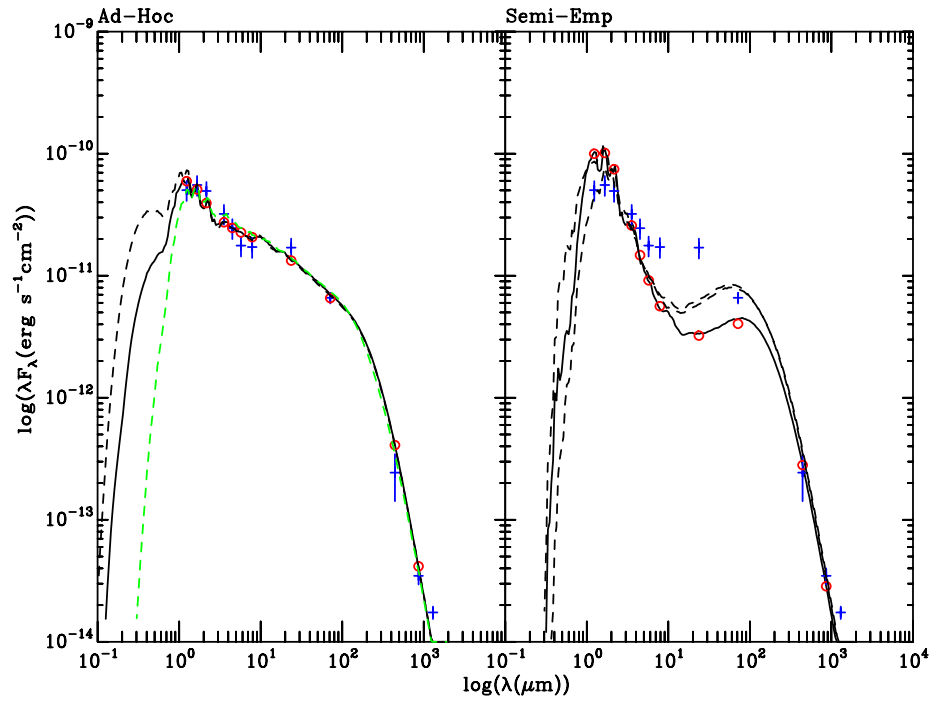


Figure 10. SEDs and monochromatic fluxes for BDD164 where symbols have the same meanings as Figure 2.

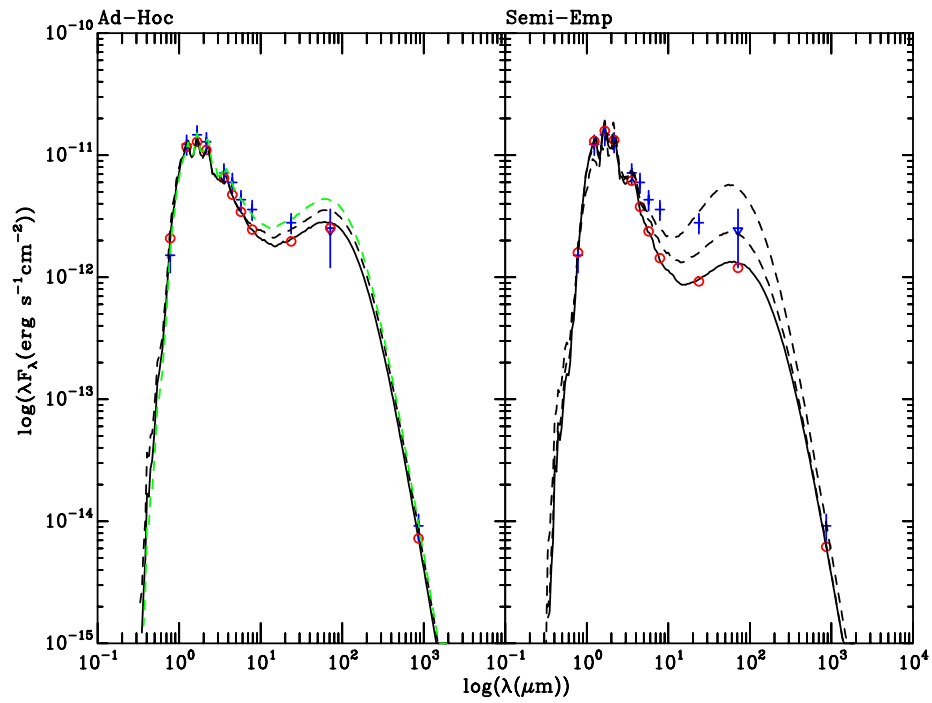


Figure 11. SEDs and monochromatic fluxes for BDD304 where symbols have the same meanings as Figure 2.

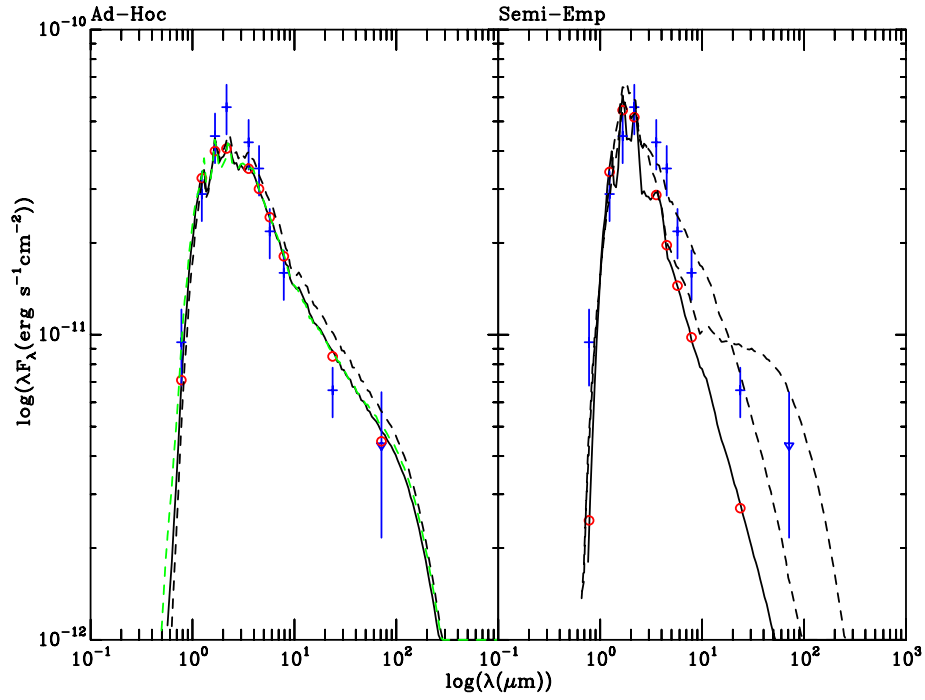


Figure 12. SEDs and monochromatic fluxes for GM Tau where symbols have the same meanings as Figure 2.

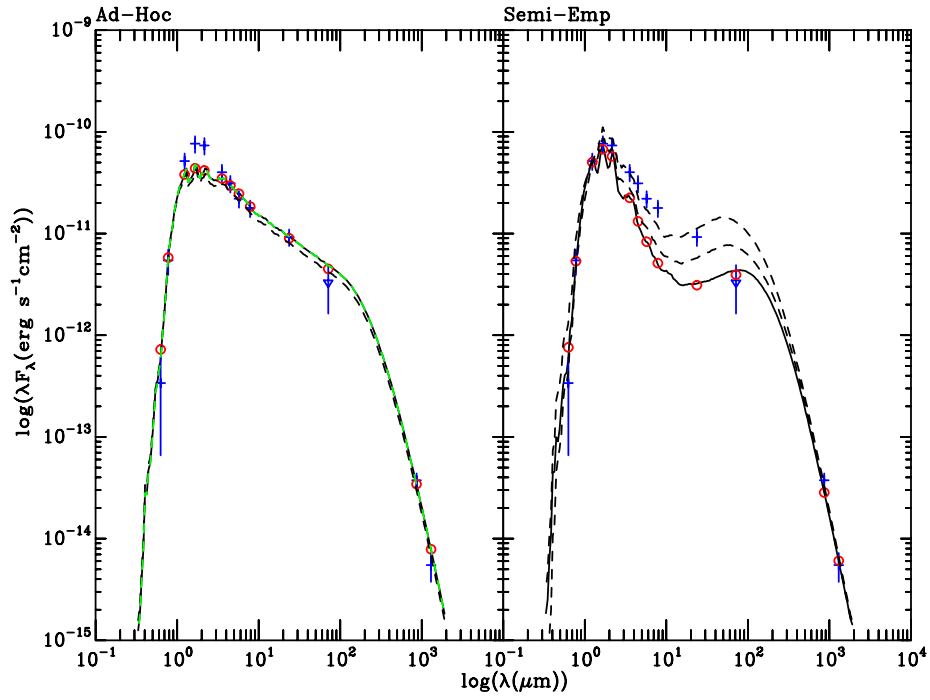


Figure 13. SEDs and monochromatic fluxes for CFHT-Tau 4 where symbols have the same meanings as Figure 2.

any of the accreting models (see Figure 13). However, our derived accretion rate, $\log \dot{M} = -9_{-3.00}^{+0.14}$ is consistent with the literature value of -11.3 Muzerolle et al. (2005), whilst our best fitting model accretion rate is significantly elevated ($\log \dot{M} = -9$). We again derive a best fitting disc mass of $M_{\text{disc}} = 0.01 M_{\odot}$.

Whilst many stars have evidence of lower accretion rates as presented in Table 7, BDD164 was found to have a lower accretion rate, $\log \dot{M} = -11.03$, and subsequently Bouy et al. (2008) derived a much higher accretion rate of $\log \dot{M} = -9.7$ using SED fitting. Therefore, within our uncertainties we are unable to rule out the higher accretion rates based on the values presented in Table 7, and more work must be done to ascertain whether SED fitting in general overestimates the accretion rates of BDD targets, or whether other methods systematically underestimate the accretion rates.

5 ADOPTED PARAMETERS

Adopting realistic uncertainties for the distance and extinction, as oppose to fixing them, does not result in significant variation in the best fitting parameters (as shown in Section 4). As there is no physical reason to assume all objects in Taurus are at 140 pc, and that the extinctions derived in the literature are infinitely precise, we have adopted the fits where these parameters are varied over a reasonable range.

For the naked objects we have found that for most cases, excepting ITG 2 and CFHT-Tau 5, the SEDs are well represented and the best fitting parameters consistent with literature values, when fitting using the semi-empirical grid, (i.e. assuming negligible accretion and allowing the “model” or “isochronal” age to vary). Clearly, this variation in age simply reflects a variation in luminosity and its underlying causes are beyond the scope of this paper but are discussed in the literature (e.g. Mayne & Naylor 2008). For the cases of ITG 2 and CFHT-Tau 5 it is apparent that these objects are at luminosities elevated, for their masses, above the 1 Myr isochrone and therefore could not be fitted satisfactorily (we are running a grid to address this, see Section 6).

All of the targets with discs, BDDs, were best fit using the accreting models of the ad-hoc grid, with the exception of CFHT-Tau 12. This suggests that variations in the accretion rate and occultation by the disc are sufficient to account for the luminosity spreads in this population. Although again some objects are more luminous than the 1 Myr isochrone namely, GM Tau and CFHT-Tau 4.

The resulting adopted parameters for each BD and BDD object are included in Tables 9, 5 and 10, for naked and disc objects respectively.

6 CONCLUSIONS

We have collected a set of photometric observations for a sample of Taurus low-mass star and brown dwarf candidates. We then derived best fitting parameters and uncertainties for the stellar and disc properties (if required). We have shown that most naked brown dwarfs in Taurus can be fit using negligibly accreting models over a range of ages, with the exception of ITG 2 and CFHT-Tau 5 where the stars were found to be over-luminous when compared to the

1 Myr isochrone. For targets with a disc we found satisfactory fits and derived a new list of accretion rates for all targets using accreting models with an age of 1 Myr. The only exception is CFHT-Tau 12 where a different age, amongst small adjustments to other parameters, yielded a better fit. Additionally, we have shown that changes in the disc structure can combine in complex ways to reproduce the SEDs of the brown dwarf and disc objects but with significantly different geometrical, e.g. inner disc position, properties to those found in the literature. As we have allowed the disc structure (in the ad-hoc grid) to adjust to an equilibrium state using a more realistic, vertical structure we favour our best fitting models. We have included physical mechanisms which are largely accepted for CTTS systems, in the ad-hoc grid. If the BD regime is a mere extension of CTTS physical regime to lower masses these mechanism will govern the structure of BDD systems. So, by comparing these models with observations we are discovering limitations in our theoretical models, which directs improvements. On the other-hand fitting such systems using models with parameterisations, although it leads to acceptable fits and predicted parameters may, obscure problems with our understanding of this regime. Therefore, we would encourage fitting of observations using models derived using robust physical ingredients, as opposed to fitting to large grids constructed by adopting significant parameterisation, given the degenerate nature of SED fitting for BD and BDD objects.

The models presented in this paper have been incorporated into an online fitting tool. This tool currently allows users to select from two models grids to which observations can be fitted. However, the fitting tool itself is independent of these grids and simply requires a structured list of SEDs in order for observations to be fitted to any new model grid. We are currently running a further model grid to expand the parameter space covered and address some of the issues with the over- or under-luminous sources (when compared to the isochrones). It is our hope that continued development of the models of LMS and BD stars with discs will be informed by feedback from fitting tools such as the one presented in this paper.

We have attempted to publish a complete description of our techniques on <http://bd-server.astro.ex.ac.uk/> allowing users and researchers to recreate, check and compare to what we have done.

7 ACKNOWLEDGMENTS

The calculations for this paper were performed on the DiRAC Facility jointly funded by STFC, the Large Facilities Capital Fund of BIS, and the University of Exeter. NJM and TJH were supported by STFC grant ST/F003277/1.

REFERENCES

- Acreman D. M., Harries T. J., Rundle D. A., 2010, MNRAS, 403, 1143
- Allard F., Hauschildt P. H., Schweitzer A., 2000, ApJ, 539, 366
- Asplund M., Grevesse N., Sauval A. J., 2006, Communications in Asteroseismology, 147, 76

- Baraffe I., Chabrier G., Allard F., Hauschildt P. H., 1998, *A&A*, 337, 403
- Bertout C., Robichon N., Arenou F., 1999, *A&A*, 352, 574
- Bessell M. S., 2000, *PASP*, 112, 961
- Bessell M. S., 2005, *ARA&A*, 43, 293
- Bessell M. S., Brett J. M., 1988, *PASP*, 100, 1134
- Bessell M. S., Castelli F., Plez B., 1998, *A&A*, 333, 231
- Bouvier J., Covino E., Kovo O., Martin E. L., Matthews J. M., Terranegra L., Beck S. C., 1995, *A&A*, 299, 89
- Bouy H., Huélamo N., Pinte C., co authors ., 2008, *A&A*, 486, 877
- Briceño C., Luhman K. L., Hartmann L., Stauffer J. R., Kirkpatrick J. D., 2002, *ApJ*, 580, 317
- Burningham B., Naylor T., Littlefair S. P., Jeffries R. D., 2005, *MNRAS*, 356, 1583
- Camenzind M., 1990, in Klare G., ed., *Reviews in Modern Astronomy Vol. 3 of Reviews in Modern Astronomy, Magnetized Disk-Winds and the Origin of Bipolar Outflows..* pp 234–265
- Carpenter J. M., Hillenbrand L. A., Skrutskie M. F., 2001, *AJ*, 121, 3160
- Cash W., 1979, *ApJ*, 228, 939
- Chabrier G., Baraffe I., Allard F., Hauschildt P., 2000, *ApJ*, 542, 464
- Clarke C. J., Pringle J. E., 2006, *MNRAS*, 370, L10
- Cohen M., Wheaton W. A., Megeath S. T., 2003, *AJ*, 126, 1090
- Da Rio N., Robberto M., Soderblom D. R., Panagia N., Hillenbrand L. A., Palla F., Stassun K. G., 2010, *ApJ*, 722, 1092
- Dougados C., Ménard F., Cuillandre J.-C., Cuillandre J.-C., Magnier E., Lai O., Manset N., Fahlman G., Forveille T., Martin P., Veillet C., Bouvier J., 2001, in T. Montmerle & P. André ed., *From Darkness to Light: Origin and Evolution of Young Stellar Clusters Vol. 243 of Astronomical Society of the Pacific Conference Series, A Search for Substellar-Mass Objects in Taurus: A Deep Wide-Field Imaging Survey with the CFH12K Camera.* pp 499–+
- Dullemond C. P., Dominik C., Natta A., 2001, *ApJ*, 560, 957
- Elias J. H., Frogel J. A., Matthews K., Neugebauer G., 1982, *AJ*, 87, 1029
- Fukugita M., Ichikawa T., Gunn J. E., Doi M., Shimasaku K., Schneider D. P., 1996, *AJ*, 111, 1748
- Griffin M., Swinyard B., Vigroux L., co authors ., 2008, in *Society of Photo-Optical Instrumentation Engineers (SPIE) Conference Series Vol. 7010 of Presented at the Society of Photo-Optical Instrumentation Engineers (SPIE) Conference, Herschel-SPIRE: design, ground test results, and predicted performance*
- Griffin M. J., Abergel A., Abreu A., co authors ., 2010, *ArXiv e-prints*
- Guieu S., Dougados C., Monin J.-L., Magnier E., Martín E., 2005, *MmSAI*, 76, 253
- Guieu S., Dougados C., Monin J.-L., Magnier E., Martín E. L., 2006, *A&A*, 446, 485
- Guieu S., Pinte C., Monin J., Ménard F., Fukagawa M., Padgett D. L., Noriega-Crespo A., Carey S. J., Rebull L. M., Huard T., Guedel M., 2007, *A&A*, 465, 855
- Harries T. J., 2000, *MNRAS*, 315, 722
- Harries T. J., Monnier J. D., Symington N. H., Kurosawa R., 2004, *MNRAS*, 350, 565
- Hauschildt P. H., Allard F., Ferguson J., Baron E., Alexander D. R., 1999, *ApJ*, 525, 871
- Hawarden T. G., Leggett S. K., Letawsky M. B., Ballantyne D. R., Casali M. M., 2001, *MNRAS*, 325, 563
- Hayes D. S., 1985, in D. S. Hayes, L. E. Pasinetti, & A. G. D. Philip ed., *Calibration of Fundamental Stellar Quantities Vol. 111 of IAU Symposium, Stellar absolute fluxes and energy distributions from 0.32 to 4.0 microns.* pp 225–249
- Herbst W., Eislöffel J., Mundt R., Scholz A., 2007, in Reipurth B., Jewitt D., Keil K., eds, *Protostars and Planets V The Rotation of Young Low-Mass Stars and Brown Dwarfs.* pp 297–311
- Herczeg G. J., Hillenbrand L. A., 2008, *ApJ*, 681, 594
- Holland W. S., Robson E. I., Gear W. K., Cunningham C. R., Lightfoot J. F., Jenness T., Ivison R. J., Stevens J. A., Ade P. A. R., Griffin M. J., Duncan W. D., Murphy J. A., Naylor D. A., 1999, *MNRAS*, 303, 659
- Indebetouw R., Mathis J. S., co authors ., 2005, *ApJ*, 619, 931
- Jayawardhana R., Ardila D. R., Stelzer B., Haisch Jr. K. E., 2003, *AJ*, 126, 1515
- Jayawardhana R., Coffey J., Scholz A., Brandeker A., van Kerkwijk M. H., 2006, *ApJ*, 648, 1206
- Jeffries R. D., Littlefair S. P., Naylor T., Mayne N. J., 2011, *MNRAS*, 418, 1948
- Johnson H. L., 1966, *ARA&A*, 4, 193
- Kennedy G. M., Kenyon S. J., 2009, *ArXiv e-prints*
- Klein R., Apai D., Pascucci I., Henning T., Waters L. B. F. M., 2003, *ApJL*, 593, L57
- Koenigl A., 1991, *ApJL*, 370, L39
- Konopacky Q. M., Ghez A. M., Rice E. L., Duchêne G., 2007, *ApJ*, 663, 394
- Kraus A. L., Hillenbrand L. A., 2007, *ApJ*, 662, 413
- Kraus A. L., Hillenbrand L. A., 2009, *ApJ*, 704, 531
- Kurosawa R., Harries T. J., Bate M. R., Symington N. H., 2004, *MNRAS*, 351, 1134
- Landolt A. U., 1992, *AJ*, 104, 340
- Littlefair S. P., Naylor T., Mayne N. J., Saunders E., Jeffries R. D., 2011, *MNRAS*, 413, L56
- Lucy L. B., 1999, *A&A*, 344, 282
- Luhman K. L., 2004, *ApJ*, 617, 1216
- Luhman K. L., Adame L., D’Alessio P., Calvet N., McLeod K. K., Bohac C. J., Forrest W. J., Hartmann L., Sargent B., Watson D. M., 2007, *ApJ*, 666, 1219
- Luhman K. L., Allen P. R., Espaillat C., Hartmann L., Calvet N., 2010, *ApJS*, 186, 111
- Luhman K. L., Hernández J., Downes J. J., Hartmann L., Briceño C., 2008, *ApJ*, 688, 362
- Luhman K. L., Lada C. J., Hartmann L., Muench A. A., Megeath S. T., Allen L. E., Myers P. C., Muzerolle J., Young E., Fazio G. G., 2005, *ApJL*, 631, L69
- Luhman K. L., Whitney B. A., Meade M. R., Babler B. L., Indebetouw R., Bracker S., Churchwell E. B., 2006, *ApJ*, 647, 1180
- Martín E. L., Dougados C., Magnier E., Ménard F., Magazzù A., Cuillandre J.-C., Delfosse X., 2001, *ApJL*, 561, L195
- Mayne N. J., Harries T. J., 2010, *MNRAS*, 409, 1307
- Mayne N. J., Naylor T., 2008, *MNRAS*, 386, 261
- Mayne N. J., Naylor T., Littlefair S. P., Saunders E. S., Jeffries R. D., 2007, *MNRAS*, 375, 1220

- Min M., Dullemond C. P., Dominik C., de Koter A., Hovenier J. W., 2009, *A&A*, 497, 155
- Mohanty S., Shu F. H., 2008, *ApJ*, 687, 1323
- Monin J., Guieu S., Pinte C., Rebull L., Goldsmith P., Fukagawa M., Ménard F., Padgett D., Stappelfeld K., McCabe C., Carey S., Noriega-Crespo A., Brooke T., Huard T., Terebey S., Hillenbrand L., Guedel M., 2010, *ArXiv e-prints*
- Monnier J. D., Millan-Gabet R., 2002, *ApJ*, 579, 694
- Muzerolle J., Hillenbrand L., Calvet N., Briceño C., Hartmann L., 2003, *ApJ*, 592, 266
- Muzerolle J., Luhman K. L., Briceño C., Hartmann L., Calvet N., 2005, *ApJ*, 625, 906
- Naylor T., Jeffries R. D., 2006, *MNRAS*, 373, 1251
- Neugebauer G., Habing H. J., van Duinen R., co authors ., 1984, *ApJL*, 278, L1
- Olofsson J., Augereau J., van Dishoeck E. F., Merín B., Grosso N., Ménard F., Blake G. A., Monin J., 2010, *A&A*, 520, A39+
- Pinte C., Harries T. J., Min M., Watson A. M., Dullemond C. P., Woitke P., Ménard F., Durán-Rojas M. C., 2009, *A&A*, 498, 967
- Poglitsch A., Waelkens C., Bauer O. H., co authors ., 2008, in *Society of Photo-Optical Instrumentation Engineers (SPIE) Conference Series Vol. 7010 of Presented at the Society of Photo-Optical Instrumentation Engineers (SPIE) Conference, The Photodetector Array Camera and Spectrometer (PACS) for the Herschel Space Observatory*
- Poglitsch A., Waelkens C., Geis N., co authors ., 2010, *ArXiv e-prints*
- Reach W. T., Megeath S. T., Cohen M., Hora J., Carey S., Surace J., Willner S. P., Barmby P., Wilson G., Glaccum W., Lowrance P., Marengo M., Fazio G. G., 2005, *PASP*, 117, 978
- Rieke G. H., Lebofsky M. J., 1985, *ApJ*, 288, 618
- Robitaille T. P., Whitney B. A., Indebetouw R., Wood K., 2007, *ApJS*, 169, 328
- Robitaille T. P., Whitney B. A., Indebetouw R., Wood K., Denzmore P., 2006, *ApJS*, 167, 256
- Scholz A., Jayawardhana R., Wood K., 2006, *ApJ*, 645, 1498
- Siess L., Dufour E., Forestini M., 2000, *A&A*, 358, 593
- Simons D. A., Tokunaga A., 2002, *PASP*, 114, 169
- Skrutskie M. F., Cutri R. M., Stiening R., co authors ., 2006, *AJ*, 131, 1163
- Stauffer J. R., Hartmann L. W., Fazio G. G., Allen L. E., Patten B. M., Lowrance P. J., Hurt R. L., Rebull L. M., Cutri R. M., Ramirez S. V., Young E. T., Rieke G. H., Gorlova N. I., Muzerolle J. C., Slesnick C. L., Skrutskie M. F., 2007, *ApJS*, 172, 663
- Stephens D. C., Leggett S. K., 2004, *PASP*, 116, 9
- Tannirkulam A., Harries T. J., Monnier J. D., 2007, *ApJ*, 661, 374
- Tannirkulam A., Monnier J. D., Harries T. J., Millan-Gabet R., Zhu Z., Pedretti E., Ireland M., Tuthill P., ten Brummelaar T., McAlister H., Farrington C., Goldfinger P. J., Sturmman J., Sturmman L., Turner N., 2008, *ApJ*, 689, 513
- Tokunaga A. T., Simons D. A., Vacca W. D., 2002, *PASP*, 114, 180
- Torres R. M., Loinard L., Mioduszewski A. J., Rodríguez L. F., 2009, *ApJ*, 698, 242
- Walker C., Wood K., Lada C. J., Robitaille T., Bjorkman J. E., Whitney B., 2004, *MNRAS*, 351, 607
- Watson A. M., Stappelfeldt K. R., 2007, *AJ*, 133, 845
- White R. J., Basri G., 2003, *ApJ*, 582, 1109
- Whitney B. A., Indebetouw R., Bjorkman J. E., Wood K., 2004, *ApJ*, 617, 1177
- Wood K., Wolff M. J., Bjorkman J. E., Whitney B., 2002, *ApJ*, 564, 887
- Zacharias N., Monet D. G., Levine S. E., Urban S. E., Gaume R., Wycoff G. L., 2005, *VizieR Online Data Catalog*, 1297, 0

Data Units	Av	R	I	J	H	K	L	[3.6]	[4.5]	[5.8]	[8.0]	24	70 mJy	450	850	1300
1 σ (default)	0.8	0.8	0.3										Upper limits (<) assumed as 2 σ , otherwise stated.			
Sources without infrared excess																
KPNO-Tau 4	2.45	20.54	18.75	15.00	14.02	13.28	12.60	12.56	12.35	12.23	12.11	<0.89 (mJy)	<57.20			-1.58 \pm 0.90
CFHT-Tau 15	1.30		17.94	14.93	14.24	13.69	13.20	13.20	13.05	12.98	13.00	<0.89 (mJy)	<57.20			-0.69 \pm 0.75
KPNO-Tau 5	0.00	19.10	15.08	12.64	11.92	11.54	10.83	11.05	10.92	10.81	10.85	<0.89 (mJy)	<57.20			
CFHT-Tau 16	1.51		17.91	14.96	14.25	13.70	13.21	13.21	13.11	13.03	13.02	<0.89 (mJy)	<57.20			
CFHT-Tau 13	3.49		17.90	14.83	13.97	13.45	12.85	12.75	12.73	12.67	12.67	<1.20 (mJy)	<72.20			
CFHT-Tau 7	0.00	16.63	14.12	11.54	10.79	10.40	9.91	9.79	9.74	9.72	9.69	9.69	<134.00			
CFHT-Tau 5	9.22	23.37	18.79	13.96	12.22	11.28	10.42	10.19	10.08	10.05	10.05	9.81	<57.20			
CFHT-Tau 11	0.00		14.88	12.53	11.94	11.59	11.19	11.19	11.06	11.02	10.98	<0.89 (mJy)				
KPNO-Tau 9	0.00		18.76	15.49	14.76	14.17	13.03	13.61	13.53	13.44	13.48	<0.89 (mJy)				-2.62 \pm 0.82
CFHT-Tau 2	0.00	20.21	16.81	13.76	12.76	12.17	11.57	11.57	11.38	11.37	11.36	<0.89 (mJy)	<65.90		<5.81	-0.60 \pm 0.80
CFHT-Tau 3	0.00	20.33	16.88	13.72	12.84	12.37	11.77	11.77	11.62	11.56	11.54	<0.89 (mJy)				0.37 \pm 0.77
ITG 2	0.64	20.21	14.71	11.55	10.63	10.10	9.57	9.42	9.33	9.34	9.34	9.25	<79.00			-0.46 \pm 0.80
Sources with infrared excess																
CFHT-Tau 9	0.91		15.35	12.88	12.19	11.76		11.11	10.80	10.48	9.85	6.79	<57.20			
KPNO-Tau 6	0.88	20.56	17.90	15.00	14.20	13.69	12.60	13.08	12.77	12.41	11.82	9.10 \pm 0.22	<75.80			-0.66 \pm 0.79
KPNO-Tau 7	0.00		17.16	14.52	13.83	13.27	12.35	12.60	12.27	11.93	11.26	8.44	<57.20			0.70 \pm 0.88
CFHT-Tau 12	3.44		16.26	13.15	12.15	11.55		10.77	10.54	10.31	9.93	8.25				
BDD399	0.00	20.33	17.84	15.18	14.13	12.98		10.79	10.14	9.61	8.91	5.03	<70.70			2.29 \pm 0.75
GM Tau	4.34		15.04	12.80	11.59	10.63		9.44	8.95	8.64	7.97	5.33	<103.00			
CFHT-Tau 6	0.41	18.39	15.40	12.65	11.84	11.37		10.78	10.37	10.03	9.16	6.44				2.86 \pm 0.76
CFHT-Tau 4	3.00	19.10	15.64	12.17	11.01	10.33		9.51	9.08	8.63	7.85	4.96	<77.80		10.8 \pm 1.8	2.38 \pm 0.75
CFHT-Tau 8	1.80	19.27	16.43	13.19	12.12	11.45		10.85	10.23	9.86	9.14	6.53	<57.20			
BDD304	1.06		17.03	13.73	12.80	12.22		11.38	10.87	10.40	9.59	6.26	<57.20		2.64 \pm 0.64	
BDD164	0.00			12.20	11.36	10.76		9.75	9.34	8.87	7.89	4.30	157.00 \pm 15.7	36 \pm 15	10 \pm 1.5	7.55 \pm 0.89

Table 2. The adopted photometry and extinctions (A_v , Guieu et al. 2005, 2006, 2007) for each target. R and I photometry are from CFHT12K and MEGACAM and are sourced from Martin et al. (2001), Luhman (2004) and Guieu et al. (2006). The JHK magnitudes are from 2MASS. L band observations are presented in Jayawardhana et al. (2003). The IRAC photometry has been published in Luhman et al. (2006), Guieu et al. (2007), Monin et al. (2010) and Luhman et al. (2010). MIPs photometric magnitudes are from Luhman et al. (2010) and the monochromatic fluxes from Guieu et al. (2007). The SCUBA 450 and 850 data are from Klein et al. (2003) and the 1300 μ m fluxes are from Klein et al. (2003) and Scholz et al. (2006). For MIPs 24 μ m column contains magnitudes unless denoted with (mJy) where a flux in mJy is given. < denotes upper limits (in mJy) which are assumed to be 2 σ upper limits. The uncertainties presented in the third row are adopted unless a specific uncertainty is stated with the observation. The division of sources with and without infrared excess is from Guieu et al. (2007).

Name	Spectral Type (SpT) (± 0.5 unless stated (1,3,7))	A_V (± 0.8 unless stated (1,3,7))	T_{eff} (K)	Mass (M_{\odot})	$\log\left(\frac{L_{\text{bol}}}{L_{\odot}}\right)$
Sources without infrared excess					
KPNO-Tau 4	M9.50(1,2,4,5,6,7,8), M9.75(3)	2.45(1), 2.5(3,7)	2360(3), 2300(4)	0.011(4), 0.014(5), 0.012(8)	-2.138(3), -2.638(4)
CFHT-Tau 15	M8.25(1,7,8)	1.30(1,7)		0.027(7)	
KPNO-Tau 5	M7.50(1,2,5,6,8) ($\pm 0.25(2)$)	0.0(1), 1.30(6)**		0.052(5), 0.044(8)	
CFHT-Tau 16	M8.50(1,7,8)	1.51(1,7)		0.022(8)	
CFHT-Tau 13	M7.25(1,7,8)	3.49(1,7)		0.051(8)	
CFHT-Tau 7B	M6.50(1,3,7,8,9), M5.75(10)	0.0(1,3,7)	2833(3)	0.07(9), 0.078(8)	-0.976(3)
CFHT-Tau 5	M7.50(1,3,7)	9.22(1,3,7)	2688(3)	0.044(8)	-0.877(3)
CFHT-Tau 11	M6.75(1,7,8)	0.0(1,7)		0.068(8)	
KPNO-Tau 9	M8.50(1,2,5,6,8) ($\pm 0.25(2)$)	0.0(1), 9.07(6)**		0.026(5), 0.022(8)	
CFHT-Tau 2	M7.50(1,2,6,8) ($\pm 0.25(2)$), M8(2,5,11)	0.0(1,11), 1.99(2)*	2795(2)	0.036(5), 0.044(8)	
CFHT-Tau 3	M7.75(1,2,4,6,8) ($\pm 0.25(2)$), M9(2,5,11)	0.0(1,11), 0.99(2)*	2752(2)	0.038(8), 0.035(4), 0.016(5)	-2.056(4)
ITG 2	M7.25(1,5,12)	0.64(1), 0.60(12)*	2838(12)	0.065(5), 0.051(8)	-1.222(12)
Sources with infrared excess					
CFHT-Tau 9	M6.25(1,7,8), M5.75 $\pm 0.25(10)$	0.91(1,7), 0.50(10)	2959(1,7), 3020 $\pm 35(10)$	0.09(8), 0.087 $^{+0.012(10)}$ $_{-0.01}$	-1.644 $M(10)$
KPNO-Tau 6	M9.0(3,7), M8.5(2,4,6,8,10) ($\pm 0.25(2,10)$)	0.88(1,7), 0.90(10), 7.6(6)**	2469(3), 2571(7), 2555(4,8) ($\pm 78(8)$)	0.022(8), 0.021 $^{+0.007(10)}$ $_{-0.007}$, 0.025(4), 0.026(5)	-2.460 $M(10)$, -2.274(3), -2.678(4)
KPNO-Tau 7	M8.25(1,2,4,5,6,8,19) ($\pm 0.25(2,10)$)	0.0(1,10), 4.07(6)**	2630 $\pm 578(10)$, 2632(4)	0.027(8), 0.03(4,5,10) ($^{+0.12(10)}$ $_{-0.14}$)	-2.482(4), -2.364 $M(10)$
CFHT-Tau 12	M6.50(1,7,8)	3.44(1,7)	2924(7)	0.078(8)	
BDD399	M7.25(1,4,5,7,8,12)	0.0(1,12)	2838(4)	0.05(13), 0.051(7), 0.065(5), 0.07(4)	-2.745(4), -1.222(13)
GM Tau	M6.50(1,7,8,10,12) ($\pm 0.5(10)$)	4.34(1), 4.08(12)*	2935(10,12) ($\pm 55(10)$)	0.078(7), 0.074 $^{+0.015(10)}$ $_{-0.013}$	-1.328(12), -1.452 $M(10)$
CFHT-Tau 6	M7.25(1,3,4,5,7,12), M8.25(8)	0.4(3), 0.41(1,7), 0.25(12)*	2838(12), 2818(7), 2724(3)	0.051(8), 0.050(4), 0.065(5)	-1.699(12), -1.383(3), -1.721(4)
CFHT-Tau 4B	M7.00(1,3,4,5,8,10,11,12) ($\pm 0.25(10)$)	3.0(1), 2.48(12)*	2880(12,10) ($\pm 33(10)$)	0.058(8), 0.06(4), 0.068 $^{+0.012(10)}$ $_{-0.007}$	-1.268(12), -1.092 $M(10)$
CFHT-Tau 8	M5.5(12), M6.50(1,3,7,8)	1.8(1,3), 1.77(7), 2.48(12)*	3058(12), 2833(3), 2924(7)	0.078(8)	-1.620(12), -1.455(3)
BDD304	M7.75(1,4,5,8,12)	1.06(1), 0.99(12)*	2752(4,12)	0.035(4), 0.038(8), 0.04(5)	-2.036(12), -2.066(4)
BDD164	M7.25(1,5,8,9,10,12) ($\pm 0.25(10)$)	0.0(1,12,10)(1)	2838(12), 2840 $\pm 43(10)$	0.051(8), 0.054 $^{+0.008(10)}$ $_{-0.008}$	-1.553(12), -1.432 $M(10)$

Table 4. A table of the stellar properties, either derived or adopted, for the sample of BDs with and without infrared excesses (as defined by Guieu et al. 2007). References: (1) Guieu et al. (2007), (2) Briceño et al. (2002), (3) Guieu et al. (2005), (4) Muzerolle et al. (2006), (5) Scholz et al. (2006), (6) Jayawardhana et al. (2003), (7) Guieu et al. (2006), (8) Kraus & Hillenbrand (2007), (9) Konopacky et al. (2007), (10) Kraus & Hillenbrand (2009), (11) Martín et al. (2001), (12) Luhman (2004) and (13) Luhman et al. (2007). * denotes A_V values derived from A_J values using the extinction relations of Rieke & Lebofsky (1985). ** denotes A_V values derived from E(K-L) using relations of Rieke & Lebofsky (1985). M , column four, denotes an approximate L_{bol} derived from M_{bol} . B, column one, denotes a possible binary system (Kraus & Hillenbrand 2009).

Target Name	CFHT- Tau 16	CFHT- Tau 15	CFHT- Tau 13	CFHT- Tau 11	CFHT- Tau 7	CFHT- Tau 5 (*)	CFHT- Tau 3	CFHT- Tau 2	KPNO- Tau 9	KPNO- Tau 5	KPNO- Tau 4	ITG 2 (*)
Variable	Independent Variables											
Mass (M_{\odot})	$0.040^{+0.000}_{-0.010}$	$0.050^{+0.000}_{-0.020}$	$0.070^{+0.000}_{-0.030}$	$0.090^{+0.000}_{-0.030}$	$0.100^{+0.000}_{-0.010}$	$0.060^{+0.000}_{-0.009}$	$0.040^{+0.020}_{-0.009}$	$0.040^{+0.020}_{-0.005}$	$0.020^{+0.010}_{-0.001}$	$0.060^{+0.019}_{-0.010}$	$0.030^{+0.020}_{-0.001}$	$0.050^{+0.010}_{-0.007}$
Age (Myr)	8^{+2}_{-7}	10^{+0}_{-9}	10^{+0}_{-9}	$4^{+0.03}_{-3}$	1^{+1}_{-0}	1^{+0}_{-0}	$4^{+0.3}_{-3}$	$4^{+0.06}_{-3}$	$2^{+8}_{-0.15}$	1^{+1}_{-0}	3^{+3}_{-1}	$^{+2}_{-0}$
Dist. (pc)	$159.75^{+3.60}_{-20.36}$	$156.25^{+8.75}_{-17.64}$	$159.75^{+5.25}_{-17.50}$	$130^{+24.91}_{0.00}$	$140.50^{+8.75}_{-10.50}$	$130^{+3.50}_{-0.00}$	$133.50^{+15.75}_{-3.50}$	$130^{+17.50}_{-0.00}$	$159.75^{+5.75}_{-17.54}$	$138.75^{+21.48}_{-8.75}$	$131.75^{+33.25}_{-1.75}$	$130^{+21.00}_{-0.00}$
A_V	$1.27^{+0.58}_{-0.48}$	$1.62^{+0.48}_{-0.53}$	$2.69^{+0.96}_{-0.00}$	$0.48^{+0.40}_{-0.20}$	$0.48^{+0.29}_{-0.32}$	$8.42^{+0.38}_{-0.00}$	$0.80^{+0.00}_{-0.32}$	$0.80^{+0.00}_{-0.34}$	$0.80^{+0.00}_{-0.48}$	$0.80^{+0.00}_{-0.24}$	$3.25^{+0.00}_{-0.64}$	$4.44^{+0.00}_{-0.14}$
Dependent Variables of Best Fitting Model												
$\log\left(\frac{L_*}{L_{\odot}}\right)$	-2.323	-2.300	-2.090	-1.622	-1.160	-1.570	-2.002	-2.002	-2.580	-1.570	-2.208	-1.730
T_{eff} (K)	2760	2826	2968	3021	3002	2887	2789	2789	2519	2887	2703	2844
$\log(g)$	4.07	4.18	4.21	3.88	3.45	3.58	3.77	3.77	3.87	3.58	3.80	3.63
R_* (R_{\odot})	0.300	0.294	0.340	0.562	0.968	0.653	0.426	0.426	0.268	0.653	0.358	0.560

Table 5. Table showing the best fitting independent (with uncertainties at the 68% confidence interval) and dependent variables for the naked objects using the semi-empirical grid and fitting using a restricted grid (using the input from Table 2 and parameter ranges from Table 4). The Objects ITG 2 and CFHT-Tau 5 are denoted with (*) as no satisfactory fit was achieved. Note the age is the model age and should not be construed as an exact age of the system. Additionally, the values of the dependent or derived variables are only for the best fitting models, strictly these should span a range of values corresponding to that covered by the independent variables.

Target Name	CFHT-Tau 12 (*)	BDD 399	BDD 304	CFHT-Tau 9	CFHT-Tau 8	CFHT-Tau 6	CFHT-Tau 4 (*)	GM Tau	KPNO-Tau 6	KPNO-Tau 7
Variable	Independent Variables									
Mass (M_{\odot})	$0.05^{+0.030}_{-0.000}$	$0.08^{+0.000}_{-0.000}$	$0.06^{+0.000}_{-0.020}$	$0.08^{+0.000}_{-0.020}$	$0.08^{+0.000}_{-0.010}$	$0.06^{+0.019}_{-0.010}$	$0.08^{+0.000}_{-0.000}$	$0.08^{+0.000}_{-0.010}$	$0.03^{+0.010}_{-0.011}$	$0.03^{+0.010}_{-0.010}$
Age (Myrs) (1)	1 (10)	1	1	1	1	1	1	1	10 (1)	1 (10)
$\log \dot{M}$	$-12^{+3.00}_{-0.00}$	$-8^{+0.07}_{-1.00}$	$-9^{+1.03}_{-1.00}$	$-9^{+0.13}_{-3.00}$	$-10^{+1.03}_{-1.00}$	$-9^{+0.06}_{-3.00}$	$-9^{+0.14}_{-3.00}$	$-8^{+0.63}_{-3.11}$	$-10^{+0.05}_{-2.00}$	$-10^{+0.90}_{-2.00}$
Period (days)	0.5 (5.0)	5.0 (0.5)	5.0 (0.5)	0.5 (5.0)	5.0 (0.5)	0.5 (5.0)	5.0	5.0 (0.5)	0.5 (5.0)	0.5 (5.0)
Coverage (%)	10 (1)	10 (1)	10 (1)	10 (1)	10 (1)	10 (1)	10 (1)	10 (1)	10 (1)	10 (1)
$M_{\text{disc}} (M_{*})^{(1)}$	0.001	0.001	0.001	0.001 (0.01)	0.001 (0.01)	0.01	0.01	0.01 (0.001)	0.001	0.001 (0.01)
$R_{\text{outer}} (\text{AU})^{(1)}$	300	100	100	100 (300)	300 (100)	300 (100)	300	300 (100)	300 (100)	100 (300)
α (0=VHE) ^(1,2)	2.25 (0)	2.10	2.25 (0)	0 (2.25)	0 (2.25)	2.25 (0)	2.10	2.10	0 (2.25)	2.25 (0)
Inclination ($^{\circ}$)	$64^{+5.87}_{-16}$	64^{+0}_{-0}	$71^{+2.17}_{-71}$	$64^{+2.59}_{-37}$	$71^{+0.76}_{-49.43}$	$48^{8.66}_{-21}$	$39^{+9.44}_{-12}$	$48^{+8.01}_{-9}$	$64^{+5.22}_{-37}$	$71^{+0.99}_{-71}$
Dist (pc)	$161.50^{+3.50}_{-31.50}$	$130.00^{+14.00}_{-0.00}$	$130.00^{+17.50}_{-0.00}$	$163.25^{+1.75}_{-33.25}$	$138.75^{+19.25}_{-8.75}$	$140.50^{+22.75}_{-9.10}$	$130.00^{+14.00}_{-0.00}$	$151.00^{+6.63}_{-17.50}$	$131.75^{+19.25}_{-1.75}$	$130.00^{+31.93}_{-0.00}$
A_V	$2.64^{+0.64}_{-0.00}$	$0.64^{+0.16}_{-0.32}$	$1.80^{+0.00}_{-0.64}$	$1.15^{+0.56}_{-0.56}$	$2.60^{+0.00}_{-0.56}$	$1.21^{+0.00}_{-0.48}$	$3.24^{+0.29}_{-0.48}$	$3.54^{+0.96}_{-0.00}$	$1.52^{+0.16}_{-0.90}$	$0.80^{+0.00}_{-0.48}$
Dependent Variables of Best Fitting Model										
$\log \left(\frac{L_*}{L_{\odot}} \right)$	-1.730	-1.340	-1.570	-1.340	-1.340	-1.570	-1.340	-1.340	-2.490	-2.130
T_{eff} (K)	2846	2941	2893	2941	2941	2893	2941	2941	2667	2703
$\log(g)$	3.63	3.50	3.58	3.50	3.50	3.58	3.50	3.50	4.05	3.72
R_* (R_{\odot})	0.569	0.829	0.658	0.829	0.829	0.658	0.829	0.829	0.270	0.398
$\log \left(\frac{L}{L_{\odot}} \right)$	-5.755	-1.782	-2.762	-2.782	-3.782	-2.762	-2.782	-1.782	-3.555	-3.780
T_{eff} (K)	2496	4044	2582	2274	1279	2582	2274	4044	2554	1847
λ_{peak} (\AA)	58452	7165	11221	12742	22659	11221	12742	7165	11345	15688
R_{sub} (R_*)	2.2	6.4	7.3	2.1	6.4	2.1	6.4	6.4	2.9	2.3

Table 6. Table showing the best fitting independent (with uncertainties at the 68% confidence interval) and dependent variables for the BDD objects using the ad-hoc grid and fitting using either a set distance (140 pc) and extinction (values from Table 2) or allowing these parameters to vary over the ranges prescribed by uncertainties, i.e. 130–165 pc for distance and $A_V \pm 0.8$. The Objects CFHT-Tau 12 is denoted with an (*) as no satisfactory fit was achieved as was found, to a lesser extent for CFHT-Tau 4 which is denoted in the same way. Additionally, the values of the dependent (or derived) variables are only for the best fitting models, strictly these should span a range of values corresponding to that covered by the independent variables. (1) These variables can take only two or three available options, i.e. Age is 1 or 10 Myrs in this grid, therefore uncertainties are meaningless we simply quote the best fitting values and if models with the alternate value were found to have χ^2 values within the 68% confidence interval their values are quoted in brackets. For example in the model age column: 1 (10) means a best fit of 1 Myr was achieved but a 10 Myr model cannot be ruled out (see Table 3 for list of available parameters). (2) The α parameter can be used to calculate the β parameter ($\alpha - \beta = -1$), a nominal value of 0 is used to denote where Vertical Hydrostatic Equilibrium (VHE) is used (see discussion in Section 3).

Target Name	CFHT- Tau 16	CFHT- Tau 15	CFHT- Tau 13	CFHT- Tau 11	CFHT- Tau 7	CFHT- Tau 5	CFHT- Tau 3	CFHT- Tau 2	KPNO- Tau 9	KPNO- Tau 5	KPNO- Tau 4	ITG 2
Mass (M_{\odot})	$0.040^{+0.000}_{-0.010}$	$0.050^{+0.000}_{-0.020}$	$0.070^{+0.000}_{-0.030}$	$0.090^{+0.000}_{-0.030}$	$0.100^{+0.000}_{-0.010}$	$0.060^{+0.000}_{-0.000}$	$0.040^{+0.020}_{-0.009}$	$0.040^{+0.020}_{-0.005}$	$0.020^{+0.010}_{-0.001}$	$0.060^{+0.019}_{-0.010}$	$0.030^{+0.020}_{-0.001}$	$0.050^{+0.010}_{-0.007}$
Age (Myrs)	8^{+2}_{-7}	10^{+0}_{-9}	10^{+0}_{-9}	$4^{+0.03}_{-3}$	1^{+1}_{-0}	1^{+0}_{-0}	$4^{+0.06}_{-3}$	$4^{+0.06}_{-3}$	2^{+8}_{-1}	1^{+1}_{-0}	3^{+3}_{-1}	1^{+2}_{-0}
Dist (pc)	$159.75^{+3.60}_{-20.36}$	$156.25^{+8.75}_{-17.64}$	$159.75^{+5.25}_{-17.50}$	$130^{+24.91}_{-40.00}$	$140.50^{+8.75}_{-10.50}$	$130^{+3.50}_{-0.00}$	$133.50^{+15.75}_{-3.50}$	$130^{+17.50}_{-0.00}$	$159.75^{+5.75}_{-17.54}$	$138.75^{+21.48}_{-8.75}$	$131.75^{+33.25}_{-0.00}$	$130^{+0.00}_{-0.00}$
A_V	$1.27^{+0.58}_{-0.48}$	$1.62^{+0.48}_{-0.53}$	$2.69^{+0.96}_{-0.00}$	$0.48^{+0.40}_{-0.20}$	$0.48^{+0.28}_{-0.32}$	$8.42^{+0.38}_{-0.00}$	$0.80^{+0.00}_{-0.32}$	$0.80^{+0.00}_{-0.34}$	$0.80^{+0.00}_{-0.48}$	$0.80^{+0.00}_{-0.24}$	$3.25^{+0.00}_{-0.64}$	$1.44^{+0.00}_{-0.14}$
Independent Variables												
Dependent Variables of Best Fitting Model												
$\log\left(\frac{L}{L_{\odot}}\right)$	-2.323	-2.300	-2.090	-1.622	-1.160	-1.570	-2.002	-2.002	-2.580	-1.570	-2.208	-1.730
T_{eff} (K)	2760	2826	2968	3021	3002	2887	2789	2789	2519	2887	2703	2844
$\log(g)$	4.07	4.18	4.21	3.88	3.45	3.58	3.77	3.77	3.87	3.58	3.80	3.63
R_* (R_{\odot})	0.300	0.294	0.340	0.562	0.968	0.653	0.426	0.426	0.268	0.653	0.358	0.560

Table 9. Table showing the adopted independent variables (with uncertainties at the 68% confidence interval) and the dependent variables of the best fitting model for the naked objects. Note the age here is the “model” or isochronal age and should not be used as the exact chronological age of the system (see discussion Mayne & Naylor 2008).

Target Name	CFHT-Tau 12 (*)	BDD 399	BDD 304	BDD 164	CFHT-Tau 9	CFHT-Tau 8	CFHT-Tau 6	CFHT-Tau 4	GM Tau	KPNO-Tau 6	KPNO-Tau 7
Variable	Independent Variables										
Mass (M_{\odot})	$0.06^{+0.030}_{-0.002}$	$0.08^{+0.000}_{-0.000}$	$0.06^{+0.000}_{-0.020}$	$0.08^{+0.000}_{-0.010}$	$0.08^{+0.000}_{-0.020}$	$0.08^{+0.000}_{-0.010}$	$0.06^{+0.019}_{-0.010}$	$0.08^{+0.000}_{-0.000}$	$0.08^{+0.000}_{-0.010}$	$0.03^{+0.010}_{-0.011}$	$0.03^{+0.010}_{-0.010}$
Age (Myrs) ⁽¹⁾	2^{+2}_{-1}	1	1	1	1	1	1	1	1	10 (1)	1 (10)
$\log M$	-12	$-8^{+0.07}_{-1.00}$	$-9^{+1.03}_{-1.00}$	$-8^{+0.55}_{-3.34}$	$-9^{+0.13}_{-3.00}$	$-10^{+1.03}_{-1.00}$	$-9^{+0.06}_{-3.00}$	$-9^{+0.14}_{-3.00}$	$-8^{+0.63}_{-3.11}$	$-10^{+0.05}_{-2.00}$	$-10^{+0.90}_{-2.00}$
Period (days) ⁽¹⁾	1	5.0 (0.5)	5.0 (0.5)	5.0	0.5 (5.0)	5.0 (0.5)	0.5 (5.0)	5.0	5.0 (0.5)	0.5 (5.0)	0.5 (5.0)
Coverage (%) ⁽¹⁾	10	10 (1)	10 (1)	1 (10)	10 (1)	10 (1)	10 (1)	10 (1)	10 (1)	10 (1)	10 (1)
$M_{\text{disc}} (M_{*})^{(1)}$	0.001	0.001	0.001 (0.01)	0.01	0.001 (0.01)	0.001 (0.01)	0.01	0.01	0.01 (0.001)	0.001	0.001 (0.01)
$R_{\text{outer}} (\text{AU})^{(1)}$	100 (50)	100	100	100	100 (300)	300 (100)	300 (100)	300	300 (100)	300 (100)	100 (300)
α (0=VHE) ⁽¹⁾	2.00 (2.10)	2.10	2.25 (0)	2.10	0 (2.25)	0 (2.25)	2.25 (0)	2.10	2.10	0 (2.25)	2.25 (0)
Inclination ($^{\circ}$)	$48^{+12.80}_{-48.00}$	64^{+0}_{-0}	$71^{+2.17}_{-71}$	0^{+56}_{-0}	$64^{+2.59}_{-37}$	$71^{+0.76}_{-49.43}$	$48^{8.66}_{-21}$	$39^{+9.44}_{-12}$	$48^{+8.01}_{-9}$	$64^{+5.22}_{-37}$	$71^{+0.99}_{-71}$
Dist. (pc)	$140.50^{+24.50}_{-7.45}$	$130.00^{+14.00}_{-0.00}$	$130.00^{+17.50}_{-0.00}$	$149.25^{+4.16}_{-9.25}$	$163.25^{+1.75}_{-33.25}$	$138.75^{+19.25}_{-8.75}$	$140.50^{+22.75}_{-9.10}$	$130.00^{+14.00}_{-0.00}$	$151.00^{+6.63}_{-7.50}$	$131.75^{+19.25}_{-1.75}$	$130.00^{+31.93}_{-0.00}$
A_V	$2.64^{+0.72}_{-0.00}$	$0.64^{+0.10}_{-0.32}$	$1.86^{+0.00}_{-0.64}$	$0.80^{+0.00}_{-0.56}$	$1.15^{+0.58}_{-0.58}$	$2.60^{+0.00}_{-0.56}$	$1.21^{+0.00}_{-0.48}$	$3.24^{+0.26}_{-0.48}$	$3.54^{+0.00}_{-0.00}$	$1.52^{+0.10}_{-0.90}$	$0.80^{+0.00}_{-0.48}$
	Dependent Variables of Best Fitting Model										
$\log \left(\frac{L}{L_{\odot}} \right)$	-1.610	-1.340	-1.570	-1.340	-1.340	-1.340	-1.570	-1.340	-1.340	-2.490	-2.130
$T_{\text{eff}} (\text{K})$	2887	2941	2893	2941	2941	2941	2893	2941	2941	2667	2703
$\log(g)$	3.62	3.50	3.58	3.50	3.50	3.50	3.58	3.50	3.50	4.05	3.72
$R_{*} (R_{\odot})$	0.624	0.829	0.658	0.829	0.829	0.829	0.658	0.829	0.829	0.270	0.398
$\log \left(\frac{L}{L_{\odot}} \right)$	-	-1.7818	-2.7617	-1.7818	-2.7818	-3.7818	-2.7617	-2.7818	-1.7818	-3.5545	3.7804
$T_{\text{eff}} (\text{K})$	-	4044	2582	7192	2274	1279	2582	2274	4044	2554	1847
$\lambda_{\text{peak}} (\text{\AA})$	-	7165	11221	4029	12742	22659	11221	12742	7165	11345	15688
$R_{\text{sub}} (R_{*})$	3.5	6.4	7.3	6.4	2.1	6.4	2.1	6.4	6.4	2.9	2.3

Table 10. Table showing the adopted independent (with uncertainties at the 68% confidence interval) and dependent variables for the BDD objects. Note the age here is the “model” or isochronal age and should not be used as the exact chronological age of the system (see discussion Mayne & Naylor 2008). These objects have all been fitted using the ad-hoc grid, except for CFHT-Tau 12. (1) These variables can take only two or three available options, i.e. Age is 1 or 10 Myrs in this grid, therefore uncertainties are meaningless we simply quote the best fitting values and if models with the alternate value were found to have χ^2 values within the 68% confidence interval their values are quoted in brackets. For example in the model age column: 1 (10) means a best fit of 1 Myr was achieved but a 10 Myr model cannot be ruled out (see Table 3 for list of available parameters). The α parameter can be used to calculate the β parameter ($\alpha-\beta=-1$), a nominal value of 0 is used to denote where Vertical Hydrostatic Equilibrium (VHE) is used (see discussion in Section 3).

APPENDIX A: DATA PROBLEMS

We attempted initial fitting of the observations using the associated uncertainties quoted in the source publications for the photometry. During this fitting, the optical photometry clearly contributed a disproportionate statistical weight to the fitting process. This resulted in best fitting SEDs which were systematically shifted away from the IR and NIR observations. Previous studies have dealt with this issue by simply neglecting the shortwave, optical photometry during the fitting process (Guieu et al. 2007). However, given the powerful constraint such observations can provide on the stellar photosphere we feel such observations must be retained, where possible.

This initial fitting essentially adopted uncertainties based on a frequentist statistical approach, where we assume that the observation recorded is a value drawn from an underlying distribution. The shape of this distribution is determined by the properties of the measuring instrument and reduction or processing properties. Quoted uncertainties on observational data points are then the values encompassing 68% percent of the integrated (about the observed value) assumed or modelled Gaussian uncertainty curve. These uncertainties are by nature underestimates (encompassing 68% of the probability curve) and are to be understood as the probability that the observation, under the same exact conditions (including time), would be repeated. We adopt a Bayesian perspective whereby the uncertainties are a property of the model not the data. Such uncertainties must include a component accounting for poor or incomplete model formulation, and a component accounting for uncertainties in conversion of the model to the observational domain. In effect we are asking which model, from our set, provides the best representation of the data, as oppose to, from which model distribution are the data most likely drawn. In practice, it was clear from the initial fits that the quoted observational uncertainties were insufficient to account for all sources of discrepancy between the model and observations, particularly for the optical regime. The resulting best fitting models were systematically shifted towards the shortwave length observations leading to a shift away from the longer wavelength points. Therefore, by adjusting the uncertainties iteratively with the fitting process, for the entire sample, we constructed a representative model of the total uncertainty for each photometric regime, short, mid and long wavelength (these are presented in Table 2). Practically, this resulted in a significant widening of the quoted photometric uncertainties, which was most extreme for the optical photometry.

In this study we have combined many disparate sources of photometry using different optical equipment (telescopes, cameras and filters) spread over several epochs, whilst the models are time independent. We have also combined several model formulations, for instance models of the stellar interiors, atmospheres and models of radiative transfer in discs. Therefore, our combined uncertainties, applied to our models, will have several contributions. In this section we explore some of the underlying contributions to observational uncertainties in each photometric regime.

A0.4 IRAC Photometry

For the IRAC photometry an uncertainty of 0.2 mags was found to best represent the required uncertainties. Is this reflected by investigation of the data? Tables A1 and A2 show IRAC photometry for each target object, as published in several studies, for objects in our sample both without and with discs respectively. In almost all cases the magnitudes of the IRAC photometry vary over at most four observations, much more than the quoted uncertainties. In some cases the differences could be attributed to improved reductions (e.g. Luhman et al. 2006, 2010), whilst in others new observations have been performed (e.g. Luhman et al. 2006; Monin et al. 2010). In either case it is clear that the natural variation in such photometry is around a factor ten larger than the quoted uncertainties. Some of this variation will be caused by temporal changes in the structure of the associated disc, as demonstrated by the fact that the dispersion of the photometry is generally less for naked stars (Table A1) than those with discs (Table A2). However, there is still variation in naked stars in excess to the quoted uncertainties, which could be due to variations in the stellar emission. Even without natural variation in the photometric magnitudes it is clear that when combining several sets of photometric observations (even using the same instrument) one may expect a variation in the magnitudes larger than the quoted uncertainties. Indeed, a value of 0.2 for the approximate uncertainty across the sample is not inconsistent with the spread of magnitudes shown in Table A1 and A2.

A0.5 JHK Photometry

For the JHK photometry we found an uncertainty of 0.2 mags to best represent the combined uncertainties of the models. However, in almost all the sources quoted in the caption of Table 2 the JHK magnitudes were consistent, this is as they are all taken from the 2MASS catalogue. However, one would expect temporal variation in the JHK photometry of ~ 0.2 mag over the timescale of a few days, as shown by Carpenter et al. (2001). Therefore, when combining the JHK observations with non-contemporaneous observations, reflecting the star-and disc properties at a different time, this variation must be incorporated into the uncertainties.

A0.6 Optical Photometry

The final regime where we must model our uncertainties is in the optical. Photometry in bands shortward of *R* and *I* proved impossible to include in the fitting. The associated uncertainties required to create a sensible weighting between such observations and longer wavelength magnitudes, resulted in these observations providing no real constraint to the fit. For observations in the *R* and *I* bands uncertainties, again for the entire sample, of 0.8 and 0.3 mags respectively were found to result in the most appropriately weighted fits.

Observations in this regime are the most uncertain due to the relatively cool effective temperatures of BDs and LMS (compared to MS stars). These objects, therefore, appear faint at these wavelengths observations in optical filters are difficult to obtain with any precision. Additionally, cool atmospheres contain many more molecular species and current atmospheric models are known to include incomplete lists

Name	[3.6]	[4.5]	[5.8]	[8.0]	Sources
Magnitudes					
KPNO-Tau 4	12.49±0.04	12.34±0.06	12.20±0.06	12.11±0.06	Luhman et al. (2006)
	12.52	12.34	12.14	12.10	Guieu et al. (2007)
	12.57	12.37	12.21	12.08	Monin et al. (2010)
~ Δ	12.56±0.02	12.35±0.02	12.23±0.04	12.11±0.04	Luhman et al. (2010)
	0.08	0.03	0.09	0.03	
CFHT-Tau 15	13.17±0.03	13.06±0.07	12.95±0.06	12.86±0.10	Luhman et al. (2006)
	13.19	13.16	13.04	13.04	Guieu et al. (2007)
	13.24	13.15	13.25	13.06	Monin et al. (2010)
~ Δ	13.20±0.02	13.05±0.02	12.98±0.04	13.00±0.07	Luhman et al. (2010)
	0.07	0.11	0.30	0.20	
KPNO-Tau 5	11.00±0.06	10.90±0.05	10.84±0.04	10.79±0.04	Luhman et al. (2006)
	11.03	10.99	10.90	10.84	Guieu et al. (2007)
	11.05	11.02	10.94	10.83	Monin et al. (2010)
~ Δ	11.05±0.02	10.92±0.02	10.81±0.03	10.85±0.03	Luhman et al. (2010)
	0.05	0.10	0.13	0.06	
CFHT-Tau 16	13.15±0.06	13.10±0.06	12.95±0.09	12.83±0.09	Luhman et al. (2006)
	13.26	13.16	13.01	12.97	Guieu et al. (2007)
	12.23	13.16	13.04	12.99	Monin et al. (2010)
~ Δ	13.21±0.02	13.11±0.02	13.03±0.05	13.02±0.06	Luhman et al. (2010)
	0.11	0.06	0.09	0.19	
CFHT-Tau 13	12.79±0.05	12.70±0.04	12.58±0.06	12.66±0.05	Luhman et al. (2006)
	12.74	12.73	12.84	12.60	Guieu et al. (2007)
	12.90	12.75	12.72	12.67	Monin et al. (2010)
~ Δ	12.85±0.02		12.73±0.04		Luhman et al. (2010)
	0.16	0.05	0.26	0.07	
CFHT-Tau 7	9.92±0.04	9.77±0.05	9.70±0.04	9.69±0.03	Luhman et al. (2006)
	9.83	9.91	9.70	9.69	Guieu et al. (2007)
	9.98	9.87	9.76	9.72	Monin et al. (2010)
~ Δ&0.15	9.91±0.02	9.79±0.02	9.74±0.03	9.72±0.03	Luhman et al. (2010)
	0.14	0.06	0.03		
CFHT-Tau 5	10.37±0.04	10.21±0.05	10.06±0.04	10.02±0.03	Luhman et al. (2006)
	10.48	10.25	10.03	10.01	Guieu et al. (2007)
	10.46	10.27	10.10	10.07	Monin et al. (2010)
~ Δ	10.42±0.02	10.19±0.02	10.08±0.03	10.05±0.03	Luhman et al. (2010)
	0.11	0.08	0.07	0.06	
CFHT-Tau 11	11.12±0.07	11.03±0.06	10.98±0.04	10.94±0.04	Luhman et al. (2006)
	11.13	11.09	10.96	10.96	Guieu et al. (2007)
	11.19	11.12	11.04	10.99	Monin et al. (2010)
~ Δ	11.19±0.02	11.06±0.02	11.02±0.03	10.98±0.03	Luhman et al. (2010)
	0.07	0.09	0.08	0.05	
KPNO-Tau 9	13.51				Guieu et al. (2007)
	13.63	13.52	13.67	13.41	Monin et al. (2010)
	13.61±0.02	13.53±0.02	13.44±0.05	13.48±0.08	Luhman et al. (2010)
~ Δ	0.12	0.01	0.23	0.07	
CFHT-Tau 2	11.62±0.05	11.38±0.05	11.35±0.04	11.29±0.03	Luhman et al. (2006)
	11.54	11.41	11.32	11.33	Guieu et al. (2007)
	11.63	11.43	11.34	11.33	Monin et al. (2010)
~ Δ	11.57±0.02	11.38±0.02	11.37±0.03	11.36±0.03	Luhman et al. (2010)
	0.09	0.05	0.05	0.07	
CFHT-Tau 3	11.71±0.05	11.62±0.05	11.54±0.04	11.56±0.04	Luhman et al. (2006)
	11.78	11.69	11.61	11.59	Guieu et al. (2007)
	11.79	11.69	11.60	11.57	Monin et al. (2010)
~ Δ	11.77±0.02	11.62±0.02	11.56±0.03	11.54±0.03	Luhman et al. (2010)
	0.08	0.07	0.07	0.05	
ITG 2	9.53±0.04	9.41±0.04	9.31±0.03	9.29±0.03	Luhman et al. (2006)
	9.56	9.45	9.31	9.28	Guieu et al. (2007)
	9.60	9.47	9.37	9.31	Monin et al. (2010)
~ Δ	9.57±0.02	9.42±0.02	9.33±0.03	9.34±0.03	Luhman et al. (2010)
	0.07	0.06	0.06	0.05	

Name	[3.6]	[4.5]	[5.8]	[8.0]	Sources
Magnitudes					
CFHT-Tau 9	11.13±0.04	10.85±0.05	10.49±0.03	9.80±0.03	Luhman et al. (2006)
	11.14	10.86	10.45	9.80	Guieu et al. (2007)
	11.16	10.88	10.51	9.83	Monin et al. (2010)
~ Δ	11.11±0.02	10.80±0.02	10.48±0.03	9.85±0.03	Luhman et al. (2010)
~ Δ	0.05	0.08	0.06	0.05	
KPNO-Tau 6	13.07±0.06	12.74±0.06	12.36±0.08	11.59±0.07	Luhman et al. (2006)
	13.08	12.79	12.47	11.68	Guieu et al. (2007)
	13.12	12.77	12.42	11.58	Monin et al. (2010)
~ Δ	13.08±0.02	12.77±0.02	12.41±0.04	11.82±0.04	Luhman et al. (2010)
~ Δ	0.05	0.05	0.11	0.23	
KPNO-Tau 7	12.54±0.04	12.23±0.03	11.89±0.05	11.24±0.02	Luhman et al. (2006)
	12.59	12.27	11.90	11.22	Guieu et al. (2007)
	12.62	12.29	11.99	11.25	Monin et al. (2010)
~ Δ	12.60±0.02	12.27±0.02	11.93±0.03	11.26±0.03	Luhman et al. (2010)
~ Δ	0.08	0.06	0.10	0.04	
CFHT-Tau 12	10.86	10.63	10.34	9.95	Monin et al. (2010)
	10.77±0.02	10.54±0.02	10.31±0.03	9.93±0.03	Luhman et al. (2010)
~ Δ	0.09	0.07	0.03	0.02	
BDD399	10.71±0.03	10.12±0.05	9.55±0.03	8.86±0.03	Luhman et al. (2006)
	10.77	10.19	9.66	8.91	Guieu et al. (2007)
	10.80	10.21	9.64	8.92	Monin et al. (2010)
~ Δ	10.79±0.02	10.14±0.02	9.61±0.03	8.91±0.03	Luhman et al. (2010)
~ Δ	0.09	0.09	0.11	0.06	
GM Tau	9.16±0.05	8.70±0.07	8.38±0.03	7.79±0.02	Luhman et al. (2006)
	9.25	8.76	8.38	7.80	Guieu et al. (2007)
	9.27	8.77	8.43	7.81	Monin et al. (2010)
~ Δ	9.44±0.02	8.95±0.02	8.64±0.03	7.97±0.03	Luhman et al. (2010)
~ Δ	0.28	0.25	0.26	0.18	
CFHT-Tau 6	10.66±0.05	10.37±0.06	9.93±0.03	9.10±0.03	Luhman et al. (2006)
	10.78±0.02	10.37±0.02	10.03±0.03	9.16±0.03	Luhman et al. (2010)
~ Δ	0.12	0.00	0.10	0.06	
CFHT-Tau 4	9.38±0.05	8.97±0.06	8.54±0.02	7.79±0.03	Luhman et al. (2006)
	9.48	9.06	8.58	7.79	Guieu et al. (2007)
	9.54	9.07	8.60	7.79	Monin et al. (2010)
~ Δ	9.51±0.02	9.08±0.02	8.62±0.03	7.85±0.03	Luhman et al. (2010)
~ Δ	0.16	0.11	0.08	0.06	
CFHT-Tau 8	10.85±0.06	10.29±0.03	9.86±0.04	9.19±0.02	Luhman et al. (2006)
	10.83	10.31	9.86	9.18	Guieu et al. (2007)
		10.23±0.02		9.14±0.03	Luhman et al. (2010)
~ Δ	0.02	0.08	0.10	0.07	
BDD304	11.38±0.05	10.85±0.04	10.40±0.04	9.52±0.03	Luhman et al. (2006)
	11.37	10.88	10.43	9.53	Guieu et al. (2007)
	11.43	10.93	10.50	9.54	Monin et al. (2010)
~ Δ		10.87±0.02		9.59±0.03	Luhman et al. (2010)
~ Δ	0.06	0.08	0.10	0.07	
BDD164	9.48±0.05	8.92±0.06	8.28±0.03	7.40±0.03	Luhman et al. (2006)
	9.51	8.99	8.33	7.40	Guieu et al. (2007)
	9.56	9.00	8.36	7.43	Monin et al. (2010)
~ Δ	9.75±0.02	9.34±0.02	8.87±0.03	7.89±0.03	Luhman et al. (2010)
~ Δ	0.27	0.32	0.59	0.49	

Table A2. IRAC photometry for our target objects with discs as reported by several studies. Δ here is the approximate range of the quoted magnitudes.

of the spectral lines, on which the opacity depends Stauffer et al. (2007). However, the most significant problem with optical photometry is uncertainty about the natural system of the observations. Small changes in the filter responses, especially for asymmetric filters such as the R filter, will lead to large changes in the derived fluxes, as the SED gradient is steep across this wavelength range.

The R and I photometry presented in Table 2 comes from four sources. Martín et al. (2001) used the CFHT 12K camera and state that they observe using the R_C, I_C filters (although the CFHT 12K camera only has Mould R, I filters). They go on to say that the photometry will be explained in further detail in Dougados et al (in preparation) which we assume refers to Dougados et al. (2001), although no further explanation is provided. Therefore, it is unclear whether these photometric observations are in the CFHT 12K-Mould R, I system or have, in some way, been transformed to the Cousins system. The transformation between photometric systems is usually done using observation of Landolt standards (Landolt 1992). However, for BDs and LMS such transforms are likely to be extremely unreliable as the SED has a steep gradient across the filter, meaning uncertainties in the filter shape will lead to large inaccuracies in the photometry. Briceño et al. (2002) observed using the KPNO I filters and calibrated this to the Cousins system using Landolt (1992) standards. Luhman (2004) observes using an I filter on the four-shooter camera at the Fred Lawrence Whipple Observatory, and employs conversions using Landolt (1992) standards. The final source is the series of papers Guieu et al. (2005), Guieu et al. (2006) and Guieu et al. (2007). Guieu et al. (2005) observe using the CFHT 12K R and I , and the Mega Prime r' and i' filters, and the calibration is not explained, suggesting that these measurements are presented in the natural systems in which they are taken. These data are extended by observations presented in Guieu et al. (2006) where observations, again using the CFHT 12K and Mega Prime systems, were combined using overlapping fields, resulting in a photometric magnitudes in the Mega Prime r' and i' system, however the magnitudes are not explicitly presented. Finally, R and I magnitudes appear in Guieu et al. (2007) where they state: “All R and I data have been transformed to the CFHT12k camera’s Cousins system (see Guieu et al. 2006; Briceño et al. 2002) before conversion to absolute fluxes.” However, the magnitudes presented in Guieu et al. (2005) match those presented (for common objects) in Guieu et al. (2007). Therefore, as no transformation or calibration to Cousins is explained in either Guieu et al. (2005) or Guieu et al. (2006) we assume that the magnitudes presented in Guieu et al. (2007) are actually in the Mega Prime r', i' system.

Table A3 shows sources and photometry for the targets where we have duplicate I band measurements (all stated to be in the Cousins I photometric system). It is clear that for stars both with and without discs large variation, as much as 0.23 mags, is apparent in the I band photometry. It is reasonable to assume that the predictive power of our models will decrease towards shorter wavelengths as the dust opacity becomes more important and the slope of the SED across the filter responses leads to an exaggeration of slight errors in the adopted response. Therefore, we conclude that a minimum of 0.2 mags could be contributed to the uncertainty budget due to variation in the photometry.

Name	R	Source
Sources without infrared excess		
KPNO-Tau 4	20.54	Guieu et al. (2006), Guieu et al. (2007)
KPNO-Tau 5	19.10	Guieu et al. (2007)
CFHT-Tau 7	16.63	Guieu et al. (2005), Guieu et al. (2007)
CFHT-Tau 5	23.37	Guieu et al. (2005)
CFHT-Tau 2	20.21	Martín et al. (2001)
CFHT-Tau 3	20.33	Martín et al. (2001)
ITG 2	20.21	Guieu et al. (2007)
Sources without infrared excess		
KPNO-Tau 6	20.56	Guieu et al. (2005), Guieu et al. (2007)
BDD399	20.33	Guieu et al. (2007)
CFHT-Tau 6	18.39	Guieu et al. (2005)
CFHT-Tau 4	19.10	Martín et al. (2001)
CFHT-Tau 8	19.27	Guieu et al. (2005), Guieu et al. (2007)

Table A4. A table showing the R band photometry and sources.

Table A4 lists the sources of the R band photometry. For the R band photometry there are no duplicates (where the photometry is from different underlying sources), so we cannot assess the uncertainty of the transforms applied (as all of the photometry is stated as having been transformed to the Cousins system). However, we can assume that the uncertainty will be significantly larger than that found for the I band photometry due to the shapes of the R band filters. Figure A1 shows the filter responses (normalised to the same scale) for the Mega Prime, CFHT and Cousins R and I filters. The shapes of the I band filters are roughly consistent with the assumption of a flat response. For the R band however there exists a longer tail (extending to 0.0 μm) in the Cousins filter (Bessell 2005). This will exacerbate problems with transformations between these filters as the slope of the SED is a sharp function of wavelength in this region (see Figure A1).

Transformations are generally performed using Landolt (1992) standards, which are unreddened main-sequence (MS) stars in a limited colour range. To demonstrate why such transforms are unreliable for BD stars we have performed a simple experiment to construct a simulated version of a transformation between the relevant photometric systems. In practice transformations are made using a conversion equation as a function of colour. Table A5 shows the simulated R and I band photometry in the Cousins, CFHT 12K and Mega Prime systems for three unreddened⁶ MS stars at colours $R_c - I_c \sim 0, 1.2$ and a pre-MS BD at 2.3 behind 2 magnitudes of extinction (typical for the targets in Taurus). The simulated photometry was created using the models of Siess et al. (2000), Chabrier et al. (2000) and Hauschildt et al. (1999). Briceño et al. (2002), for example, used the standard fields SA 95 and SA 101 to calibrate their photometry to the Cousins system. These standard fields contain MS stars covering a range of colours from ~ 0.0 to 0 1.2. Whereas, the pre-MS stars of colour 2.3 is typical of the bluest BD stars in Taurus.

Table A5 shows that if we construct transformation

⁶ at 140 pc, although distance is unimportant this has been set to the distance of Taurus for illustrative purposes

Name	I Magnitudes	Sources
Sources without infrared excess		
CFHT-Tau 2 ~ Δ	16.81	Briceño et al. (2002), Guieu et al. (2005), Guieu et al. (2007)
	16.69	Martín et al. (2001)
	0.12	
CFHT-Tau 3 ~ Δ	16.88	Briceño et al. (2002), Guieu et al. (2007)
	16.77	Martín et al. (2001)
	0.11	
Sources with infrared excess		
KPNO-Tau 6 ~ Δ	17.90	Guieu et al. (2005), Guieu et al. (2007)
	17.80	Briceño et al. (2002)
	0.10	
CFHT-Tau 6 ~ Δ	15.40	Guieu et al. (2005)
	15.63	Luhman (2004)
	0.23	
CFHT-Tau 4 ~ Δ	15.78	Luhman (2004)
	15.64	Martín et al. (2001)
	0.14	
CFHT-Tau 8 ~ Δ	16.43	Guieu et al. (2005), Guieu et al. (2007)
	16.24	Luhman (2004)
	0.19	

Table A3. Duplicate photometry for which differences are above 0.05 mag.

$R_C - I_c$	Band	Cousins	CFHT 12K	Mega Prime
pre-MS, $A_V = 2$				
~ 2.3	R	19.63	20.31	20.87
	I	17.31	17.08	17.71
	$R - I$	2.32	3.23	3.16
MS, $A_V = 0$				
~ 0	R	6.35	6.36	6.37
	I	6.37	6.38	6.37
	$R - I$	-0.02	-0.02	0.00
~ 1.2	R	10.93	11.08	11.26
	I	9.73	9.68	9.95
	$R - I$	1.20	1.40	1.31

Table A5. Table showing the simulated photometry for MS stars across a range of colours and a pre-MS BD typical of the Taurus targets.

equations (assuming a linear relationship in colour between the instrumental and calibrated magnitude) using the MS stars in the colour range usually found in the Landolt (1992) standard fields we derive (assuming a negligible airmass component)

$$I_c = I_{\text{CFHT}} - 0.009 + 0.042 \times (R_{\text{CFHT}} - I_{\text{CFHT}}) \quad (\text{A1})$$

$$I_c = I_{\text{Mega}} + 0.000 - 0.168 \times (R_{\text{Mega}} - I_{\text{Mega}}) \quad (\text{A2})$$

$$R_c = R_{\text{CFHT}} - 0.012 - 0.099 \times (R_{\text{CFHT}} - I_{\text{CFHT}}) \quad (\text{A3})$$

$$R_c = R_{\text{Mega}} - 0.020 - 0.252 \times (R_{\text{Mega}} - I_{\text{Mega}}). \quad (\text{A4})$$

These relationships would then be used to extrapolate out to the required colour for transformation of Taurus BDs. The

Band	CFHT 12K	Mega Prime
$I_{\text{transforms}}$	+0.127	-0.531
$I_{\text{simulated}}$	+0.230	-0.400
$R_{\text{transforms}}$	-0.332	-0.816
$R_{\text{simulated}}$	-0.680	-1.240

Table A6. Table showing the Δ magnitudes predicted from the transforms equations which simulate the use of Landolt (1992) standards, and the actual Δ magnitudes for a typical simulated Taurus object.

results of evaluating the transform equations and comparing to the values derived from the simulated observations are shown in Table A6.

Table A6 shows that if Landolt (1992) transforms are used we would expect the transforms to be incorrect by around ~0.1 for the I band and ~0.4–0.5 for the R band for pre-MS BDs. This is caused by the shape of the SED changing across the filter responses as one moves from MS stars to BDs. The change in SED between BDs and MS is driven by a change in the surface gravity of these objects, ~5.25 for a MS star and 3.79 for a pre-MS star at similar colours. Figure A1 shows the normalised filter responses for the I and R bands of the Cousins, CFHT 12K and Mega Prime filter systems, overlaid with SEDs of a MS BD and pre-MS BD (arbitrarily scaled) for illustrative purposes.

Figure A1 shows that the area under the filter response is similar for the I band filters but the R band Cousins filters shows a longer wavelength tail. The overlaid SEDs then show that for the MS (greater flux, or higher line) and the pre-MS the long wavelength tail of the Cousins filter becomes signif-

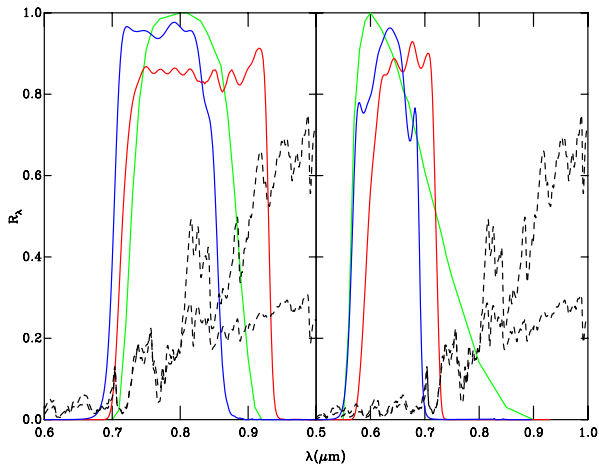


Figure A1. The normalised filters responses as a function of wavelength for the *I* (left panel) and *R* (right panel) filters of the Johnson-Cousins system (green solid line Bessell 2005), Mega Prime (blue solid lines, r' , i' of <http://cfht.hawaii.edu/Instruments/Filters/>) and CFHT 12K (red solid line, Mould *R* and *I*, <http://cfht.hawaii.edu/Instruments/Filters/>). Overlaid, normalised to arbitrary units, are the SEDs (dashed lines) of a MS (unreddened) and pre-MS ($A_V = 0$) star at a colour typical of a Taurus object ($R - I = 2.3$).

icant. This leads to the problems with transforms illustrated by Table A6. Therefore, for the *I* band photometry the combination of variations in the photometry and transformation between photometric systems, leads to an uncertainty budget of ~ 0.3 , matching the value we have adopted for the sample. For the *R* band photometry, uncertainties caused by transformations, combined with variation in the photometric magnitudes, lead to uncertainties of ~ 0.7 . However, during our fitting process we found uncertainties of 0.8 were required, suggesting that some further source of uncertainty may be required, for instance the missing opacity sources in the BD atmosphere models (Stauffer et al. 2007).

As discussed previously other authors have also tried to perform fitting using the NOMAD catalogue (Zacharias et al. 2005), which is derived from photographic plate measurements leading to extreme uncertainty in their conversion to Johnson-Cousins magnitudes, therefore as we are unsure of how to transform this photometry correctly we have not included these measurements.

Therefore, for BD objects, which have low effective temperatures (compared to MS stars), photometric transformations, within the optical regime, are likely to produce significant uncertainties in the resulting magnitudes, which are exacerbated due to the shape of the *R* filter.

APPENDIX B: CALIBRATION AND SIMULATED PHOTOMETRY

Initially, our simulated stellar photospheres were diluted by the factor $(R_*/\text{distance})^2$ to a distance of 10 pc to produce SEDs in absolute flux. These SEDs then represented simulations of ‘naked’ stars, which, as the emission is isotropic are inclination independent. For those systems where the

disc has been modelled similar absolute flux SEDs were also constructed at the inclinations detailed in Table 3.

B1 Photometric Systems and Calibration

To allow comparison and fitting to real observations these SEDs must be adjusted to account for the distance and extinction to a given target. We chose an extinction system consistent with Robitaille et al. (2007), using the same extinction curve (Indebetouw et al. 2005) interpolated onto our wavelength sampling. This allowed the construction of SEDs for stars with and without discs at any distance and extinction (using $F_{\text{app}} = F_{\text{abs}} \times 10^{(-0.4A_\lambda)} \times (\frac{10}{\text{distance(pc)}})^2$, where F_{app} is apparent flux, F_{abs} absolute flux and A_λ the extinction in the required band), for comparison to observed spectra. However, most observations of such systems are photometric and presented as either monochromatic fluxes or in a specified magnitude system. Therefore, to enable fitting we derive these photometric quantities.

To derive magnitudes one requires the underlying filter responses of the instrument, the method by which the instrument sums flux (i.e. counting photons or energy) and the assumed zero points.

The magnitudes are defined as

$$M_\lambda = -2.5 \log_{10}(N^{\text{counts}}) - \text{Zeropoint}, \quad (\text{B1})$$

where counts is usually the number of electrons, or in the case of IRAC where $\text{counts} = e^-/\text{Gain}$, as the gain is significant ($\sim 3-4$). Subsequent integration across the filter is performed as follows (as described in Bessell et al. 1998). For photon counting, i.e. responses in electrons/photon,

$$N^{\text{counts}} = \int \frac{\lambda}{hc} R_\lambda(\lambda) F_\lambda(\lambda) d\lambda \quad (\text{B2})$$

and for energy summing, i.e. responses electrons/unit energy,

$$N^{\text{counts}} = \int R_\lambda(\lambda) F_\lambda(\lambda) d\lambda \quad (\text{B3})$$

The derivation of monochromatic fluxes is explained in Appendix A of Robitaille et al. (2007). The summed flux is still calculated, as with magnitudes, but this flux is then redistributed across the filter using an underlying (well chosen) assumption as to the SEDs shape (for instance 10 000 K Black body for the *Spitzer* MIPS fluxes). Finally, the ‘‘monochromatic’’ flux is then quoted as the value of this redistributed flux curve at the central wavelength of the filter. After integration using equations B3 or B2 an additional normalisation factor is required. For a monochromatic flux,

$$\frac{\int U(\lambda) F_\lambda[\text{actual}] R_\lambda(\lambda) d\lambda}{\int R_\lambda(\lambda) d\lambda} = \frac{\int U(\lambda) F_\lambda[\text{assumed}] R_\lambda(\lambda) d\lambda}{\int R_\lambda(\lambda) d\lambda}, \quad (\text{B4})$$

where $U(\lambda)$ is 1 if the response is in e^- /unit energy or $\lambda/(h \times c)$ if the response is in e^- /photon. Then, as the assumed shape is known,

$$\lambda F_\lambda[\text{assumed}] \equiv \lambda_0 F_{\lambda_0}[\text{quoted}]. \quad (\text{B5})$$

Therefore, to correctly calibrate magnitude and monochromatic flux derivations one require the filter responses, assumed SED shape and photometric zero point. A summary

of all of the calibration information for our derived photometry is available online⁷ and is presented in Table B1. Presenting this information is vital as it means that researchers can recreate what we have done and compare quantities derived from the models with the same observational quantities regardless of the system chosen.

B2 Fitting Photometric Measurements

The derivation of magnitudes and monochromatic fluxes is performed during fitting on the apparent SEDs. At this stage the reader may ask the question why do we spend the extra computational time to derive the magnitudes and fluxes directly (at run time) from the apparent SEDs, as oppose to simply adjusting the photometry from the absolute model by the extinction and distance. Additionally, the reader might question why we derive the monochromatic fluxes so rigorously, as oppose to simply interpolating for a flux point at the assumed wavelength on the SED.

Previous fitting, in general, has been performed using these two shortcuts to provide a much faster fitting routine. However, these sacrifices imply major assumptions. Either, the filters are assumed to be infinitesimally thin, or the SED is assumed to be a smooth curve which matches the assumed SED shape across the filter as well as the filter response curves being assumed to be flat across the bandpass. In most, but not all, cases the uncertainties in the observations and data are large enough to blur any errors made due to the breakdown of these assumptions.

This breakdown is apparent for objects under heavy extinction but is perhaps best demonstrated by the use of optical photometry for BDs. In this regime the SED is a steep function of wavelength.

Most studies will convert optical magnitudes to so-called monochromatic fluxes to provide better constraint of the stellar parameters (e.g. Guieu et al. 2007; Luhman et al. 2007; Bouy et al. 2008). This conversion is usually performed by calculating a summed flux from the magnitude (i.e. reversing equation B1), then assuming some underlying SED shape (usually those presented in Table B1) and quoting the flux at the filters central wavelength. These fluxes are then fit directly to interpolated values of the flux at the same wavelength.

Figure B1 shows as solid lines the SEDs for a typical brown dwarf and disc (BDD, hereafter) model from our model grid (A model from the ad-hoc grid: $M_* = 0.04M_\odot$, Age=1 Myr, negligible accretion, a rotation period of 0.5 days, a disc mass of $0.01M_*$, a disc outer radius of 100 AU and $\alpha=2.15$), at 10 pc (left panel) and 140 pc behind an extinction of $10A_V$ (right panel). The monochromatic fluxes derived rigorously for each SED are shown for the CFHT Mega Prime u^* , g' , r' and i' filter bands (as crosses). If one applies the extinction to the monochromatic fluxes directly there results a significant difference in flux from those derived from the reddened SED. Additionally, the derived monochromatic fluxes do not lie directly on the SED, in either case. Whilst, the deviation is small given the gradient of the SED in these region the affect on the fitting statistic is significant. Essentially, if we do not derive monochromatic fluxes properly

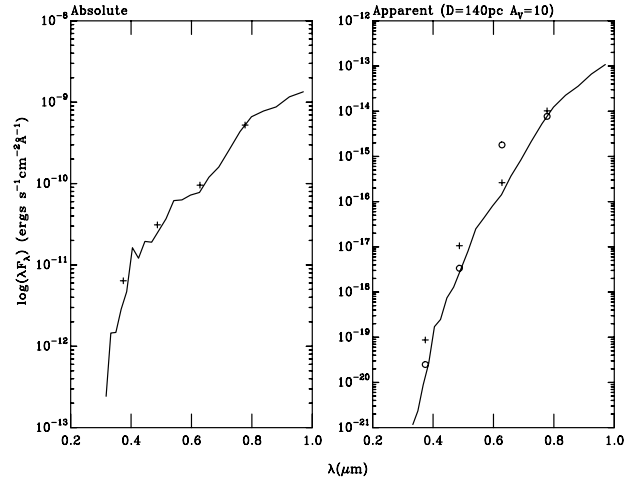


Figure B1. SEDs (solid lines) in λ (μm), λF_λ ($\text{ergs s}^{-1} \text{cm}^{-2} \text{\AA}^{-1}$), at 10 pc (left panel) and 140 pc behind an extinction of $A_V=10$ (right panel). The crosses denote the derived monochromatic fluxes for each SED and the circles on the right panel show the fluxes resulting from simply reddening the absolute monochromatic fluxes.

from the underlying SEDs, and furthermore, simply treat them as points along the SED we are not comparing two equal quantities. Therefore, for our fitting we only compare observed monochromatic fluxes with those derived from the underlying SEDs in the same way.

This problem is exacerbated in the optical regime as, due to the steep gradient across the wavelength space, the monochromatic fluxes in this region are very powerful constraints. In addition the photometric systems and conversions of these fluxes from magnitude space are often unclear or unreliable. For instance several studies have utilised the photometry of Zacharias et al. (2005) or the NOMAD survey and converted the optical magnitudes to monochromatic fluxes. However, these magnitudes are often derived from photographic plates and it is not obvious how to convert these correctly to comparable monochromatic fluxes. In fact transformations between magnitude systems are usually derived using observations of main-sequence stars and then applied, without adjustment, to LMS and BDs (this is discussed more in Section A).

A further complication for overlaying monochromatic fluxes on spectra (if one does not derive the monochromatic fluxes rigorously) is the quoted central wavelength. In reality the effective wavelength of a filter shifts position with the input spectrum as shown by Bessell et al. (1998) and is defined as,

$$\lambda_{\text{eff}} = \frac{\int \lambda F_\lambda [\text{actual}] R_\lambda(\lambda) d\lambda}{\int F_\lambda [\text{actual}] R_\lambda(\lambda) d\lambda}. \quad (\text{B6})$$

For a typical spectrum of a BD the shift in wavelength is small for filters at longer wavelengths (typically $\sim 0.01\mu\text{m}$). However, for shorter wavelength filters, where the photospheric flux changes rapidly across the filter, the shift can be as large as $\sim 0.1\mu\text{m}$. If one fits observed monochromatic fluxes to monochromatic fluxes derived for an SED in the same fashion then the effective wavelength of the filter does not affect the difference (it is just a direct comparison of

⁷ (<http://bd-server.astro.ex.ac.uk/calibration>)

fluxes). However, if the observed monochromatic flux is fitted to a simple point lying on the SED, for optical colours, then the shift in effective wavelength may well be significant, again exacerbated by the steep rise in stellar flux across the optical filters. Essentially, this leads to flux points in the optical being shifted away from the expected position. Therefore, one must be careful when overlaying optical “monochromatic fluxes” derived from optical magnitudes on model SEDs. This is discussed and an example presented in Section 4.

As the uncertainties in the models are large most previous studies have not required this level of sophistication in the derivation of photometric values. However, as this effect becomes particularly prominent in the optical the SED curve and monochromatic flux points are often dropped in this regime (see, for example, the incomplete SEDs at lower wavelengths of Guieu et al. 2007). As, using this fitting tool, we are now able to precisely model observations in the optical we no longer have this limitation and, additionally, as models improve have the software to test their predictions. Simply stated to improve the models we must ensure we are comparing them, on an equal footing, to observations.

B3 Other Tools

In addition to the fitting tool several other tools are available at <http://bd-server.astro.ex.ac.uk/> enabling users to explore the model grids. A browsing and downloading tool is available to select, view and retrieve, SEDs and flux and magnitude information for any model within any grid (<http://bd-server.astro.ex.ac.uk/plots>). Additionally, we have constructed model isochrones and mass tracks using our grids and these can be retrieved from <http://bd-server.astro.ex.ac.uk/isochrones>. Finally, we have also made available an interpolation tool allowing users to produce SEDs, monochromatic fluxes and magnitudes for models within, but not covered by, our parameter space at a user entered distance and extinction.

Filter Set	Response Units ($e^-/?$)	SED Shape (Assumed)	Zero Magnitude Flux, $F_\nu(M_0)$ (Jy)	Filter	Zero points	Central λ (μm)	Width (μm)
Johnson-Cousins (1) & (2)	Photons	Flat ⁽¹⁾	Vega ⁽²⁾	U	-14.18	0.36	0.10
				B	-15.30	0.46	0.18
				V	-14.86	0.585	0.21
				R	-15.11	0.71	0.30
				I	-14.58	0.81	0.20
				J	-14.26	1.23	0.36
				H	-13.49	1.62	0.44
				K	-13.09	2.18	0.56
Tycho (3) & (2)	Photons	Flat	Vega	V_t	-15.09	0.527	0.21
				B_t	-14.94	0.422	0.145
Bessell (4) & (5)	Photons	Flat	Vega	U	-14.23	0.37	0.11
				B	-15.32	0.44	0.18
				V	-14.86	0.55	0.21
				R	-15.09	0.64	0.29
				I	-14.57	0.80	0.20
				J	-13.92	1.22	0.36
				H	-13.65	1.63	0.96
				K	-12.71	2.19	0.36
SDSS (6) & (7)	Photons	Flat	$F_\nu(M_0)=3631$	L	-11.74	3.45	0.72
				u	-12.43	0.3555	0.0599
				g	-14.22	0.473	0.1379
				r	-14.22	0.6261	0.1382
				i	-13.78	0.7672	0.1535
2MASS (8), (9) & (10)	Photons	Flat	$F_\nu(M_0)=1594$	J	15.73	1.235	0.162
			$F_\nu(M_0)=1024$	H	16.37	1.662	0.251
			$F_\nu(M_0)=666.7$	K_S	17.38	2.159	0.262
				J	-13.48	1.24	0.16
MKO (11), (12) & (13)	Photons	Flat	Vega	H	-13.46	1.65	0.29
				K	-12.64	2.2	0.34
				Z	-13.84	0.8775	0.095
UKIRT (14), (12) & (13)	Photons	Flat	Vega	Y	-13.46	1.02	0.1
				J	-14.01	1.28	0.42
				H	-13.29	1.65	0.45
				K	-12.82	2.2	0.66
IRAS (15), (16) & (17)	Energy	Flat	$F_\nu(M_0)=28.3$	12	21.00	12.0	6.5
			$F_\nu(M_0)=6.73$	25	23.55	25.0	11.0
			$F_\nu(M_0)=1.19$	60	26.24	60.0	40.0
			$F_\nu(M_0)=0.43$	100	28.41	100.0	37.0
SCUBA ⁽⁴⁾ (18) & (19)	Energy	10 000K Black Body	N/A ⁽³⁾	450WB	0	443.0	138.92
				850WB	0	863.0	230.636
IRAC (20) & (21)	Photons	Flat	$F_\nu(M_0)=280.9$	3.6	-10.15	3.55	1.2
			$F_\nu(M_0)=179.7$	4.5	-9.70	4.493	1.56
			$F_\nu(M_0)=115.0$	5.8	-8.07	5.731	2.27
			$F_\nu(M_0)=64.9$	8.0	-8.55	7.872	4.69
MIPS (22)	Energy	10 000K Black body	$F_\nu(M_0)=7.17$	24	25.97	23.68	14.20
			$F_\nu(M_0)=0.778$	70	29.62	71.42	61.06
			$F_\nu(M_0)=0.160$	160	32.48	155.9	99.83
CIT (23) & (24)	Photons	Flat	Vega	J	-13.73	1.25	0.24
				H	-13.44	1.65	0.30
				K_S	-12.97	2.215	0.41
PACS (25), (26) & (27)	Photons	Flat	Vega	blue	-6.00	70	90.5
				green	-5.26	100	109
				red	-4.27	160	391.25
SPIRE (28), (29) & (30)	Photons	Flat	Vega	250	-3.16	250	176.30
				350	1.87	350	281.26
				500	0.0 ⁽⁵⁾	500	290.24
				V	-14.86	0.5374	0.0974
CFHT 12K (Mould) (31)	Photons	Flat	Vega				

				R	-14.69	0.6581	0.1251
				I	-14.78	0.8223	0.2164
				u*	-14.33	0.3743	0.0758
				g'	-15.49	0.4872	0.1455
CFHT Mega Prime (31)	Photons	Flat	Vega	r'	-14.76	0.6282	0.1219
				i'	-14.61	0.7776	0.1508
				z'	-15.07	1.1702	0.6868

Table B1: A table describing the calibration information for each photometric band used. Sources are given as numbers in brackets: (1) Johnson (1966), (2) Bessell (2005), (3) Bessell (2000), (4) Bessell & Brett (1988), (5) Bessell et al. (1998), (6) Fukugita et al. (1996), (7) <http://www.sdss.org/dri/algorithms/fluxcal.html>, (8) Cohen et al. (2003), (9) Skrutskie et al. (2006), (10) http://www.ipac.caltech.edu/2mass/releases/allsky/doc/sec6_4a.html, (11) Tokunaga et al. (2002), (12) Simons & Tokunaga (2002), (13) http://www.jach.hawaii.edu/UKIRT/instruments/wfcam/user_guide/description.html#Tab1.1, (14) Hawarden et al. (2001), (15) Neugebauer et al. (1984), (16) http://irsa.ipac.caltech.edu/IRASdocs/archives/spectral_resp.html, (17) <http://irsa.ipac.caltech.edu/IRASdocs/exp.sup/ch6/C2a.html>, (18) Holland et al. (1999), (19) <http://www.jach.hawaii.edu/JCMT/continuum/background/background.html>, (20) Reach et al. (2005), (21) <http://irsa.ipac.caltech.edu/data/SPITZER/docs/irac/>, (22) <http://irsa.ipac.caltech.edu/data/SPITZER/docs/mips/>, (23) Elias et al. (1982), (24) Stephens & Leggett (2004), (25) Poglitsch et al. (2008), (26) Poglitsch et al. (2010), (27) http://herschel.esac.esa.int/Docs/PACS/html/pacs_om.html, (28) Griffin et al. (2008), (29) Griffin et al. (2010), (30) http://herschel.esac.esa.int/Docs/SPIRE/html/spire_om.html#x1-880005.2.3 and (31) <http://cfht.hawaii.edu/Instruments/Filters/>. Notes are superscript numbers in bracket: (1) A Constant flux across the filter. (2) The Vega spectrum was a NextGen atmosphere model with $T_{\text{eff}}=9950\text{K}$ and $\log(g)=3.95$, scaled to the Vega flux of Hayes (1985). (4) SCUBA 2 filters approximately equal to SCUBA filters. (5) Wavelength longer than the maximum available in the Vega spectrum.